

Bifunctional Molybdenum and Vanadium Materials: Semiconductor Properties for Advanced Electronics and Catalytic Efficiency in Linalool Oxidation

Josipa Sarjanović, Mateja Cader, Edi Topić, Marta Razum, Dominique Agustin, Mirta Rubčić, Luka Pavić,* Jana Pisk*

Table of Contents

Scheme S1. Ligands used in our previous investigation (H_2L^{1*} and H_2L^{2*}) coordinated with vanadium metal centre.	4
Figure S1. IR-ATR spectra for the ligand H_2L^1	4
Figure S2. IR-ATR spectra for the ligand H_2L^2	5
Figure S3. IR-ATR spectra for the complex $[MoO_2(L^1)]_n$ (2)	5
Figure S4. IR-ATR spectra for the complex $[MoO_2(L^2)]_n$ (5)	6
Figure S5. IR-ATR spectra for the complex $[MoO_2(L^1)(H_2O)]$ (1)	6
Figure S6. IR-ATR spectra for the complex $[MoO_2(L^2)(H_2O)]$ (3)	7
Figure S7. IR-ATR spectra for the complex $[MoO_2(L^2)(MeOH)]$ (4)	7
Figure S8. DSC curve for the ligand H_2L^1	8
Figure S9. DSC curve for the ligand H_2L^2	8
Figure S10. TGA/DSC curve for the complex $[MoO_2(L^1)]_n$ (2)	9
Figure S11. TGA/DSC curve for the complex $[MoO_2(L^2)]_n$ (5)	9
Figure S12. TGA/DSC curve for the complex $[MoO_2(L^1)(H_2O)]$ (1)	10
Figure S13. TGA/DSC curve for the complex $[MoO_2(L^2)(H_2O)]$ (3)	10
Figure S14. TGA/DSC curve for the complex $[MoO_2(L^2)(MeOH)]$ (4)	11
Synthesis of side product $(pyH)_4Mo_8O_{26}$	11
Crystallographic data	12
Figure S15. Supramolecular environment in the crystal structure of $(pyH)_4(Mo_8O_{26})$. Pyridinium cations form a) normal and b) bifurcated hydrogen bonds with axial oxygen atoms of the octamolybdate anions. Atoms are shown as thermal ellipsoids with 50% probability.	12
Figure S16. (a) Molecular structure of the ligand H_2L^1 . Atoms are shown as thermal ellipsoids with 50% probability. (b) Packing of molecules in the unit cell shown along <i>a</i> -axis. (c) Supramolecular homodimers of H_2L^1 are realized through amide (C=O)-NH synthon. The same are packed in zig-zag fashion.	13
Figure S17. (a) Molecular structure of the ligand H_2L^2 . Atoms are shown as thermal ellipsoids with 50% probability. (b) Packing of molecules in the unit cell shown along <i>b</i> -axis. (c) As in H_2L^1 , supramolecular homodimers of H_2L^2 are realized through amide (C=O)-NH synthon. However, in this case the dimers form sheets <i>via</i> (C=O)-CH ₃ short contacts.	15

Figure S18. (a) Molecular structure of the complex $[\text{MoO}_2(\text{L}^1)(\text{H}_2\text{O})]$ (1). Atoms are shown as thermal ellipsoids with 50% probability. (b) Packing of molecules in the unit cell shown along *a*-axis. (c) The molecules of dioxomolybdenum(vi) complex show relatively complex supramolecular architecture, forming $R\bar{6}6(24)$ and larger supramolecular rings through $\text{O}_w\text{-H}\cdots\text{O}=\text{Mo}$ and $\text{O}_w\text{-H}\cdots\text{N}_{\text{amide}}$ hydrogen bonds. The water ligand hydrogen bond donors not participating in the supramolecular ring structure interact with neighboring complex molecules by the same motifs, forming a supramolecular net. 16

Figure S19. (a) Molecular structure of the complex $[\text{MoO}_2(\text{L}^2)(\text{H}_2\text{O})]$ (3). Atoms are shown as thermal ellipsoids with 50% probability. (b) Packing of molecules in the unit cell shown along *b*-axis. (c) Contrary to the L^1 counterpart, the molecules form supramolecular chains *via* $\text{O}_w\text{-H}\cdots\text{O}_{\text{phen}}$, $\text{O}_w\text{-H}\cdots\text{O}_{\text{methoxy}}$ and $\text{O}_w\text{-H}\cdots\text{N}_{\text{amide}}$ hydrogen bonds. The chains interact weakly through numerous $\text{Mo}=\text{O}_{\text{ax}}\cdots\text{H}-\text{C}$ contacts. 18

Figure S20. (a) Molecular structure of the complex $[\text{MoO}_2(\text{L}^2)(\text{MeOH})]$ (4). Atoms are shown as thermal ellipsoids with 50% probability. (b) Packing of molecules in the unit cell shown along *c*-axis. (c) Lacking a ditopical hydrogen bond donor, molecules of complex exclusively form non-interacting homodimers through $\text{O}_{\text{MeOH}}\text{-H}\cdots\text{N}_{\text{amide}}$ hydrogen bonds. Interestingly, the dimers form between symmetrically equivalent molecules, yielding two geometrically distinct (albeit very similar) dimer types. The dimers are bound with an assortment of weak $\text{C}-\text{H}\cdots\text{O}$ contacts. 19

Figure S21. Photos of the single crystals analysed by SCXRD: (a) $[\text{MoO}_2(\text{L}^1)(\text{H}_2\text{O})]$, (b) $[\text{MoO}_2(\text{L}^2)(\text{H}_2\text{O})]$, (c) $[\text{MoO}_2(\text{L}^2)(\text{MeOH})]$, (d) $(\text{pyH})_4\text{Mo}_8\text{O}_{26}$ 20

Table S1. Experimental and crystallographic data for crystal structures determined in this work. 21

Table S2. Selected bond lengths in the determined crystal structures. 23

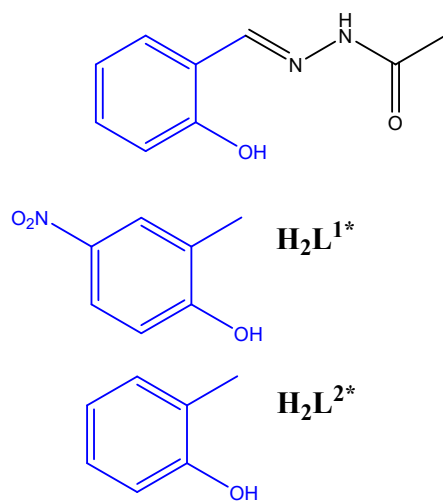
Table S3. Hydrogen bond parameters in the determined crystal structures. 24

Figure S22. Kinetic profiles of linalool conversion with (a) $[\text{MoO}_2(\text{L}^1)]_n$ (2) and $[\text{MoO}_2(\text{L}^2)]_n$ (5) and (b) $[\text{MoO}_2(\text{L}^2)(\text{MeOH})]$ (4), $[\text{MoO}_2(\text{L}^1)(\text{H}_2\text{O})]$ (1) and $[\text{MoO}_2(\text{L}^2)(\text{H}_2\text{O})]$ (3). Solid circles represent reactions with TBHP in decane, while empty circles represent reactions with TBHP in water. Blue circles represent reactions with $[\text{MoO}_2(\text{L}^2)]_n$ (5), dark red circles with $[\text{MoO}_2(\text{L}^1)]_n$ (2), orange circles with $[\text{MoO}_2(\text{L}^2)(\text{H}_2\text{O})]$ (3), green circles with $[\text{MoO}_2(\text{L}^1)(\text{H}_2\text{O})]$ (1), and purple circles with $[\text{MoO}_2(\text{L}^2)(\text{MeOH})]$ (4). 25

Figure S23. Kinetic profiles of linalool conversion with (a) $[\text{MoO}_2(\text{L}^1)]_n$ (2) and $[\text{MoO}_2(\text{L}^2)]_n$ (5) and (b) $[\text{MoO}_2(\text{L}^2)(\text{MeOH})]$ (4), $[\text{MoO}_2(\text{L}^1)(\text{H}_2\text{O})]$ (1) and $[\text{MoO}_2(\text{L}^2)(\text{H}_2\text{O})]$ (3). Solid circles represent reactions with H_2O_2 , while empty circles represent reactions with H_2O_2 with acetonitrile. Blue circles represent reactions with $[\text{MoO}_2(\text{L}^2)]_n$ (5), dark red circles with $[\text{MoO}_2(\text{L}^1)]_n$ (2), orange circles with $[\text{MoO}_2(\text{L}^2)(\text{H}_2\text{O})]$ (3), green circles with $[\text{MoO}_2(\text{L}^1)(\text{H}_2\text{O})]$ (1), and purple circles with $[\text{MoO}_2(\text{L}^2)(\text{MeOH})]$ (4). 25

Figure S24. Kinetic profiles of linalool conversion with (a) $[\text{VO}_2(\text{HL}^{1*})]$ and $[\text{VO}_2(\text{HL}^{2*})]$ and (b) $[\text{VO}(\text{L}^{1*})(\text{OMe})(\text{MeOH})]$, $[\text{VO}(\text{L}^2)(\text{OEt})(\text{H}_2\text{O})]$, and $[\text{VO}(\text{L}^2)(\text{OMe})(\text{MeOH})]$. Solid circles represent reactions with TBHP in decane, while empty circles represent reactions with TBHP in water. Dark red circles represent reactions with $[\text{VO}_2(\text{HL}^{1*})]$, blue circles with $[\text{VO}_2(\text{HL}^{2*})]$, green circles with

[VO(L ^{1*})(OMe)(MeOH)], orange circles with [VO(L ²)(OEt)(H ₂ O)], and purple circles with [VO(L ²)(OMe)(MeOH)].....	26
Figure S25. Kinetic profiles of linalool conversion with (a) [VO ₂ (HL ^{1*})] and [VO ₂ (HL ^{2*})] and (b) [VO(L ^{1*})(OMe)(MeOH)], [VO(L ²)(OEt)(H ₂ O)], and [VO(L ²)(OMe)(MeOH)]. Solid circles represent reactions with H ₂ O ₂ , while empty circles represent reactions with H ₂ O ₂ with the addition of acetonitrile. Dark red circles represent reactions with [VO ₂ (HL ^{1*})], blue circles with [VO ₂ (HL ^{2*})], green circles with [VO(L ^{1*})(OMe)(MeOH)], orange circles with [VO(L ²)(OEt)(H ₂ O)], and purple circles with [VO(L ²)(OMe)(MeOH)].	26
Table S4. Catalytic results of linalool oxidation with vanadium catalysts. The reaction was carried out at 80 °C with TBHP in decane and TBHP in water, and at 70 °C with H ₂ O ₂ . <i>n</i> (catalyst)/ <i>n</i> (linalool)/ <i>n</i> (oxidant) = 0.05 mmol/10 mmol/20 mmol.	27
Catalytic results and discussion for the vanadium catalysts.....	28
Electrical characterisation of previously reported Mo and V complexes.....	29
Table S5. Activation energy values for the DC conductivity in the cooling cycle of the prepared complexes. DC conductivity values for all compounds measured @200 °C in the cooling run.	29
Figure S26. Conductivity spectra for mononuclear [MoO ₂ (L ²)(H ₂ O)] (3) compound in heating (a) and cooling (b) runs, along with (c) Arrhenius plots for DC conductivity for both runs (red circle – heating, blue circle – cooling).	29
Figure S27. Conductivity spectra for mononuclear [MoO ₂ (L ²)(MeOH)] (4) compound in heating (a) and cooling (b) runs, along with (c) Arrhenius plots for DC conductivity for both runs (red circle – heating, blue circle – cooling).	30
Scheme S2. Structural representation of ligands H ₂ L ¹ and H ₂ L ² with NMR labels.....	30
Figure S28. ¹ H NMR spectrum of the ligand H ₂ L ¹ with an enlarged view of the signals at chemical shifts from 6.77 to 7.42 ppm	31
Figure S29. ¹³ C NMR spectra of the ligand H ₂ L ¹	31
Figure S30. ¹ H NMR spectrum of the ligand H ₂ L ² with an enlarged view of the signals at chemical shifts from 6.70 to 7.30 ppm	32
Figure S31. ¹³ C NMR spectra of the ligand H ₂ L ²	32
Scheme S3. Structural representation of the complexes [MoO ₂ (L ¹)(H ₂ O)] (1) and [MoO ₂ (L ²)(H ₂ O)] (3) with NMR labels.....	33
Figure S32. ¹ H NMR spectrum of the complex [MoO ₂ (L ¹)(H ₂ O)] (1) with an enlarged view of the signals at chemical shifts from 6.90 to 7.35 ppm.....	33
Figure S33. ¹³ C NMR spectrum of the complex [MoO ₂ (L ¹)(H ₂ O)] (1)	34
Figure S34. ¹ H NMR spectrum of the complex [MoO ₂ (L ²)(H ₂ O)] (3) with an enlarged view of the signals at chemical shifts from 6.90 to 7.30 ppm.....	34
Figure S35. ¹³ C NMR spectrum of the complex [MoO ₂ (L ²)(H ₂ O)] (3)	35



Scheme S1. Ligands used in our previous investigation (H_2L^{1*} and H_2L^{2*}) coordinated with vanadium metal centre.

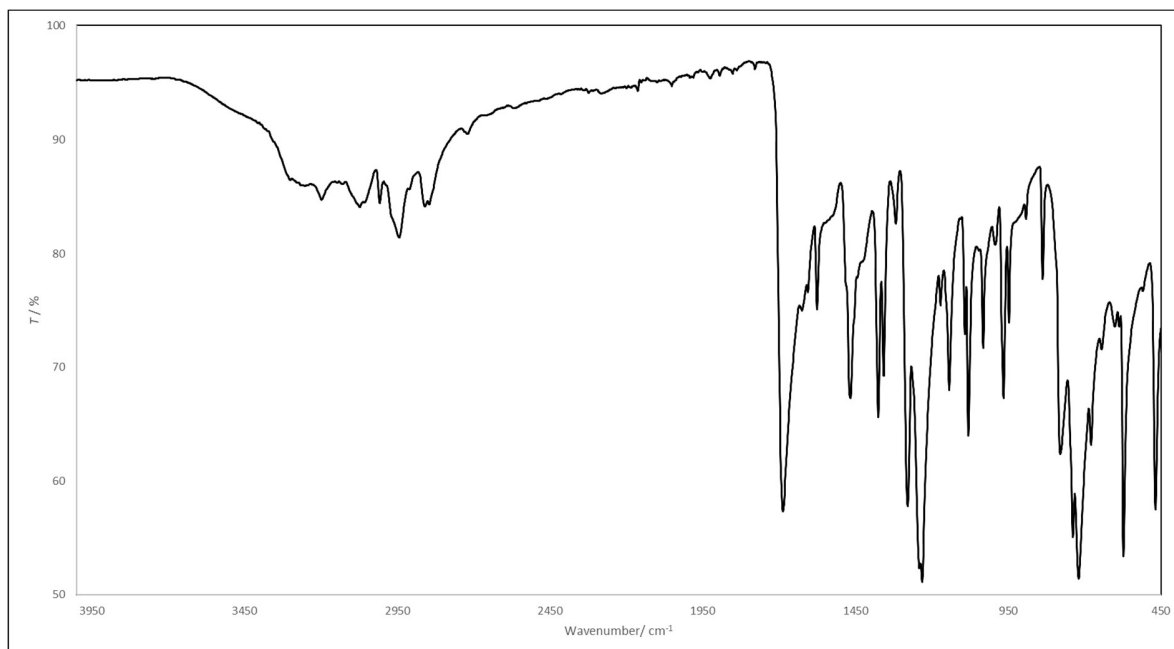


Figure S1. IR-ATR spectra for the ligand H_2L^1

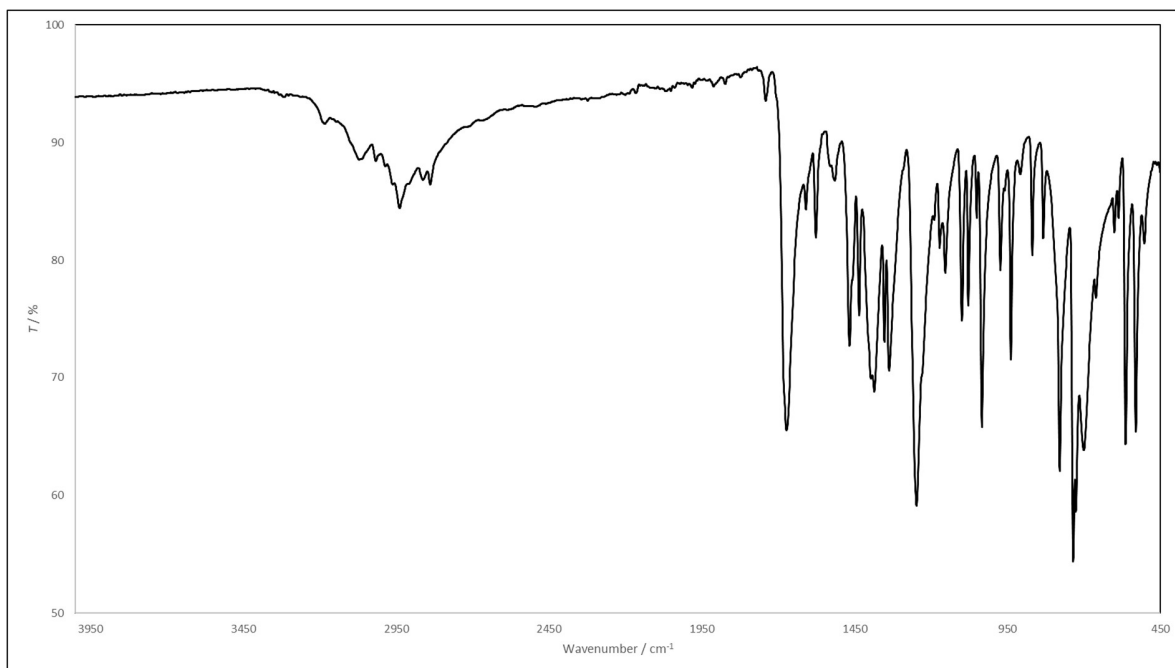


Figure S2. IR-ATR spectra for the ligand H_2L^2

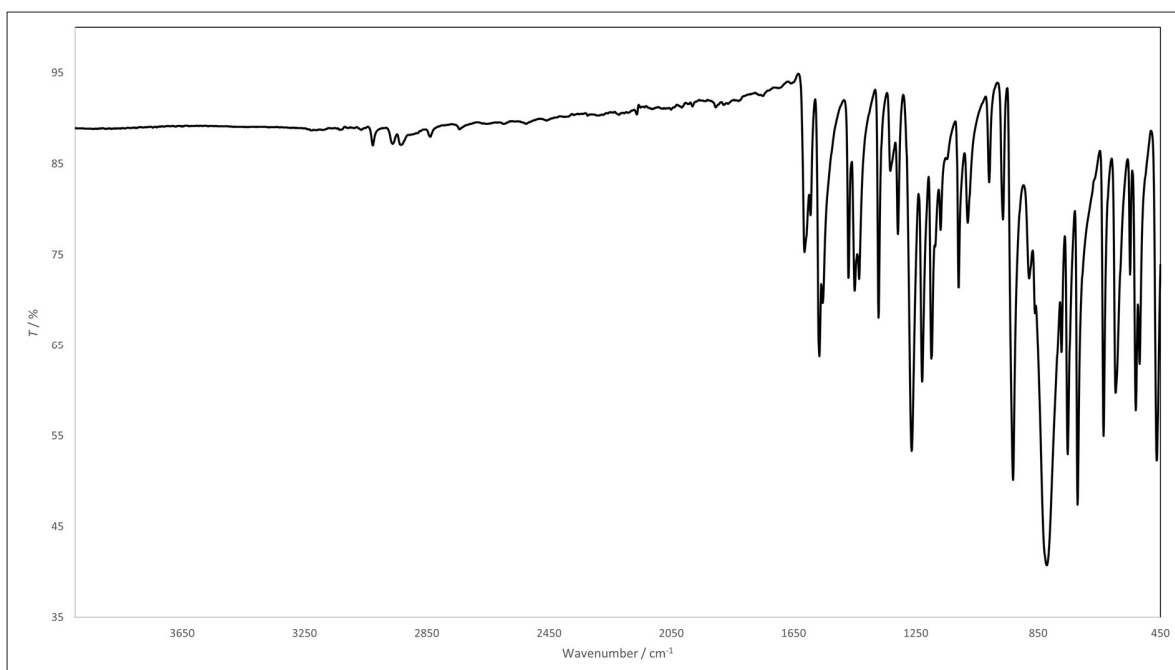


Figure S3. IR-ATR spectra for the complex $[MoO_2(L^1)]_n$ (2)

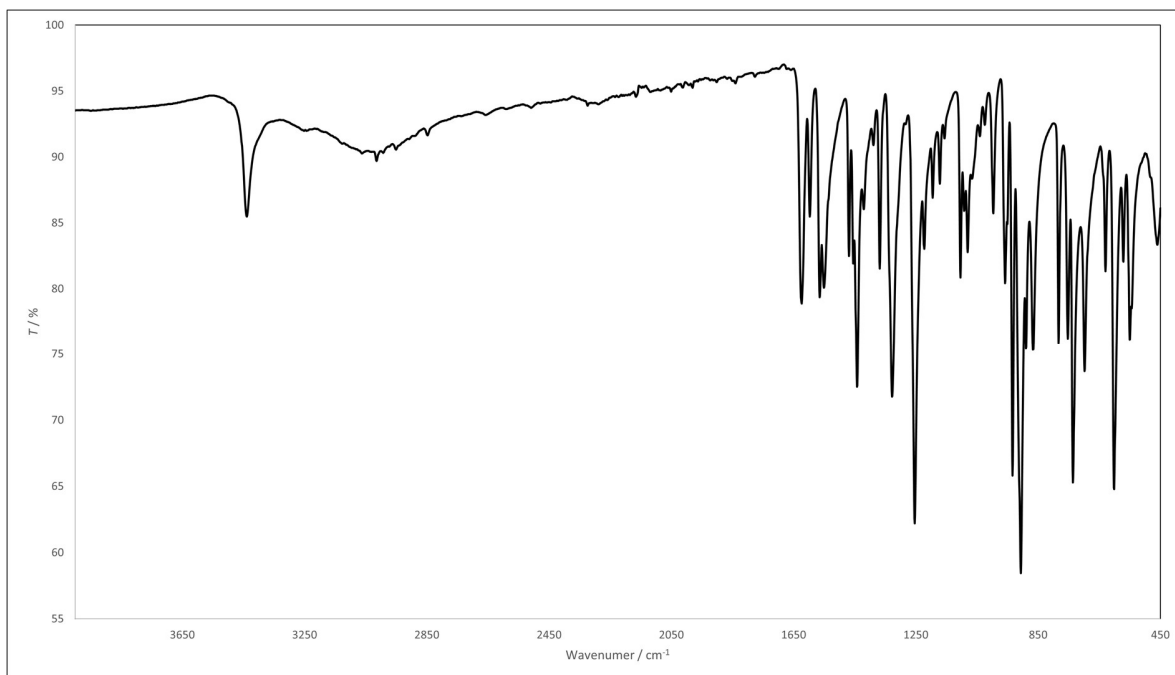


Figure S4. IR-ATR spectra for the complex $[\text{MoO}_2(\text{L}^2)]_n$ (5)

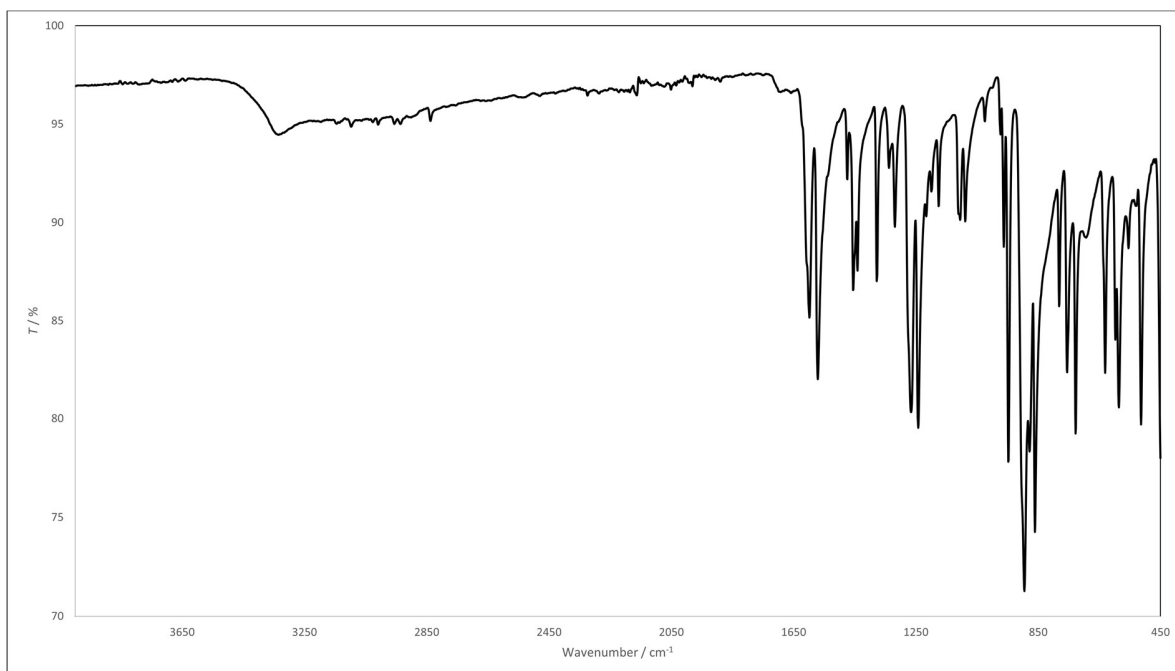


Figure S5. IR-ATR spectra for the complex $[\text{MoO}_2(\text{L}^1)(\text{H}_2\text{O})]$ (1)

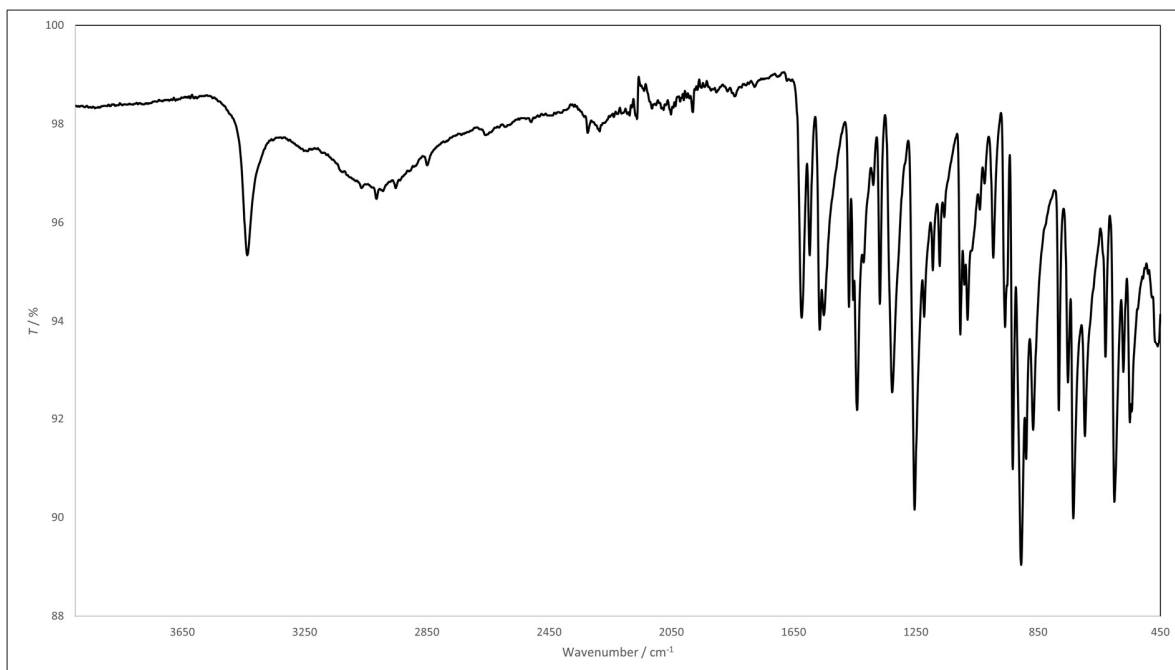


Figure S6. IR-ATR spectra for the complex [MoO₂(L²)(H₂O)] (3)

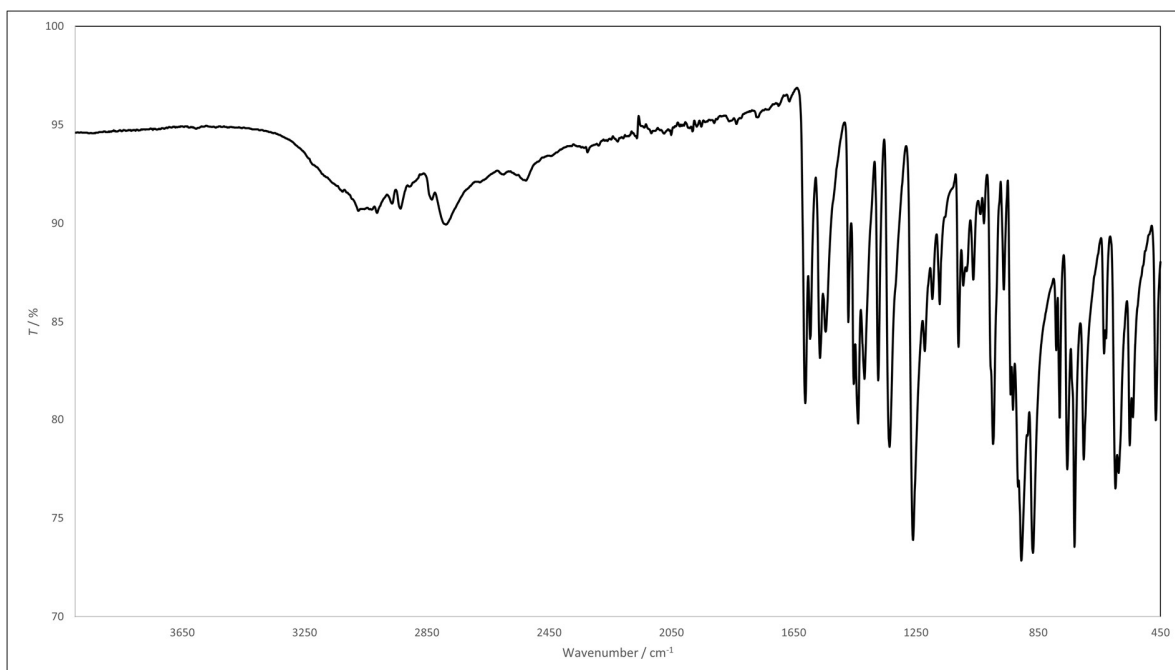


Figure S7. IR-ATR spectra for the complex [MoO₂(L²)(MeOH)] (4)

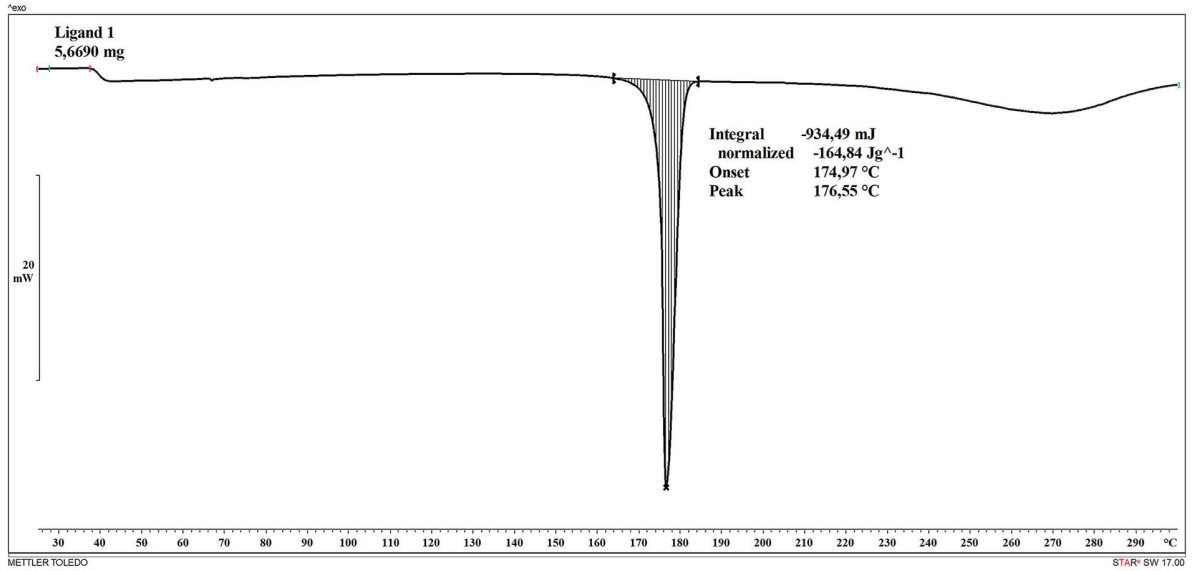


Figure S8. DSC curve for the ligand H₂L¹

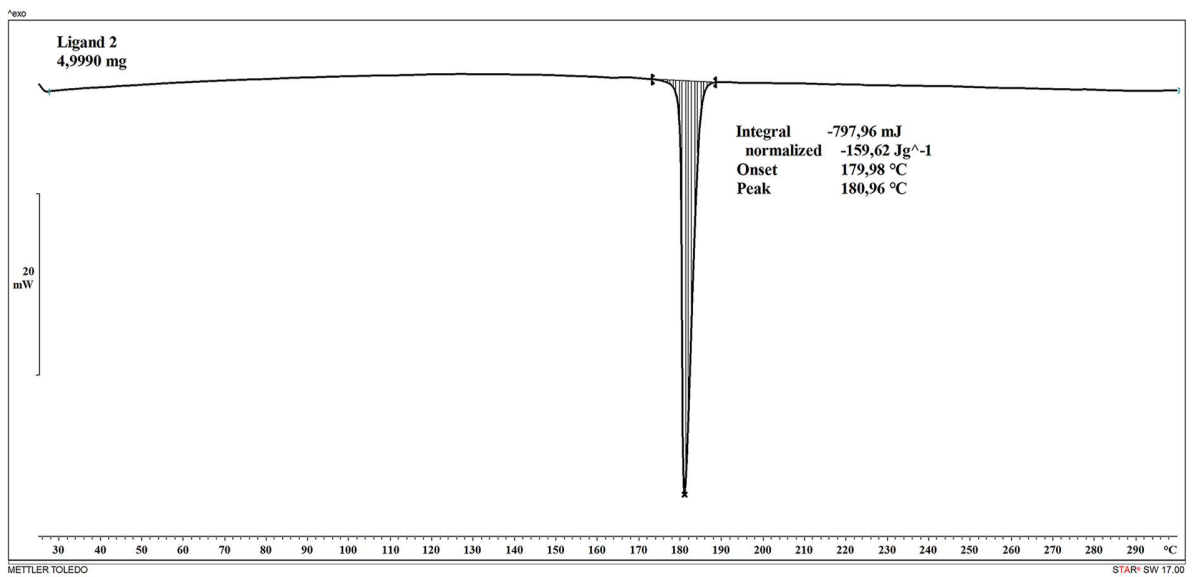


Figure S9. DSC curve for the ligand H₂L²

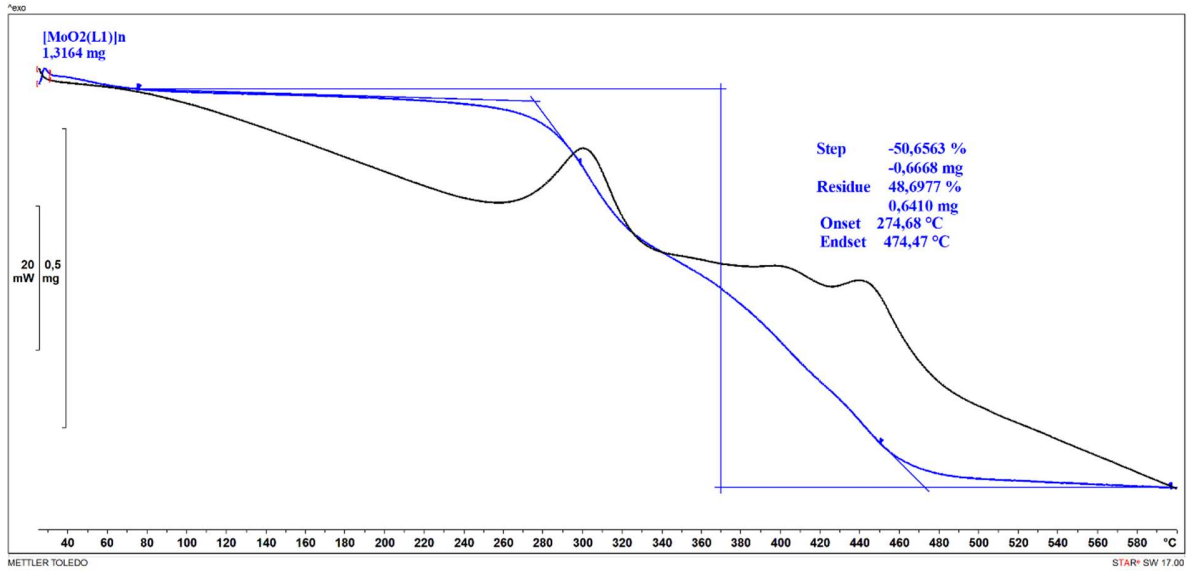


Figure S10. TGA/DSC curve for the complex [MoO₂(L¹)]_n (2)

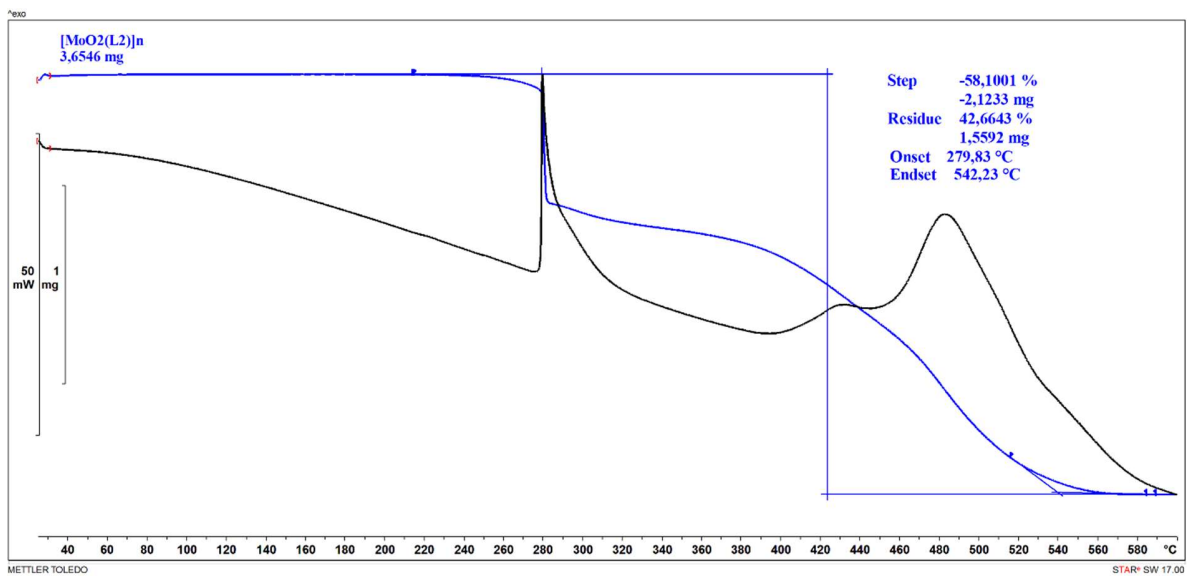


Figure S11. TGA/DSC curve for the complex [MoO₂(L²)]_n (5)

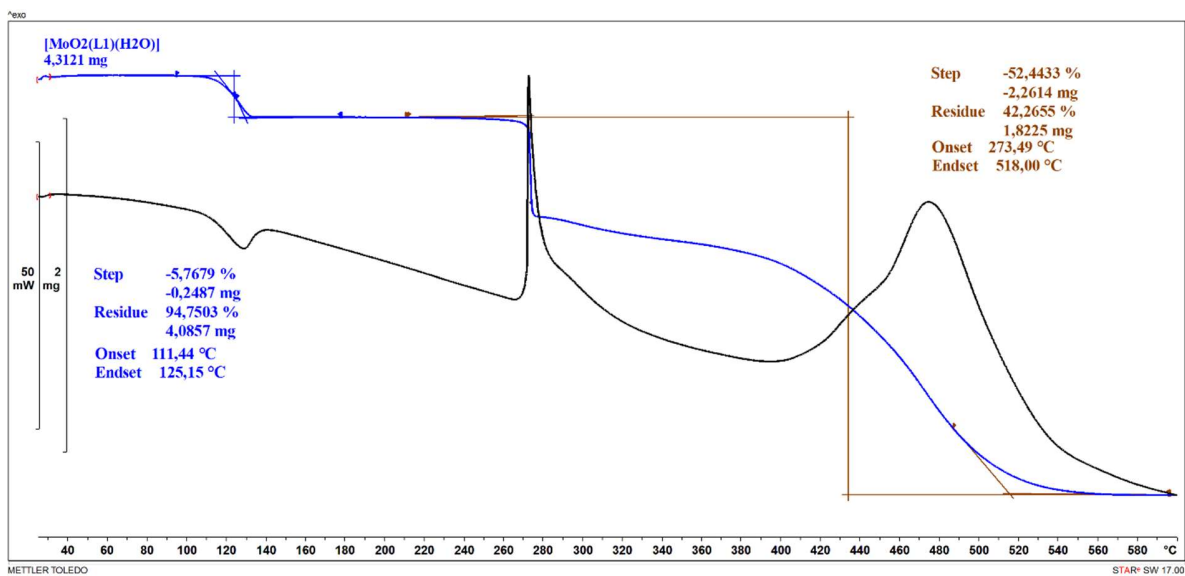


Figure S12. TGA/DSC curve for the complex [MoO₂(L¹)(H₂O)] (1)

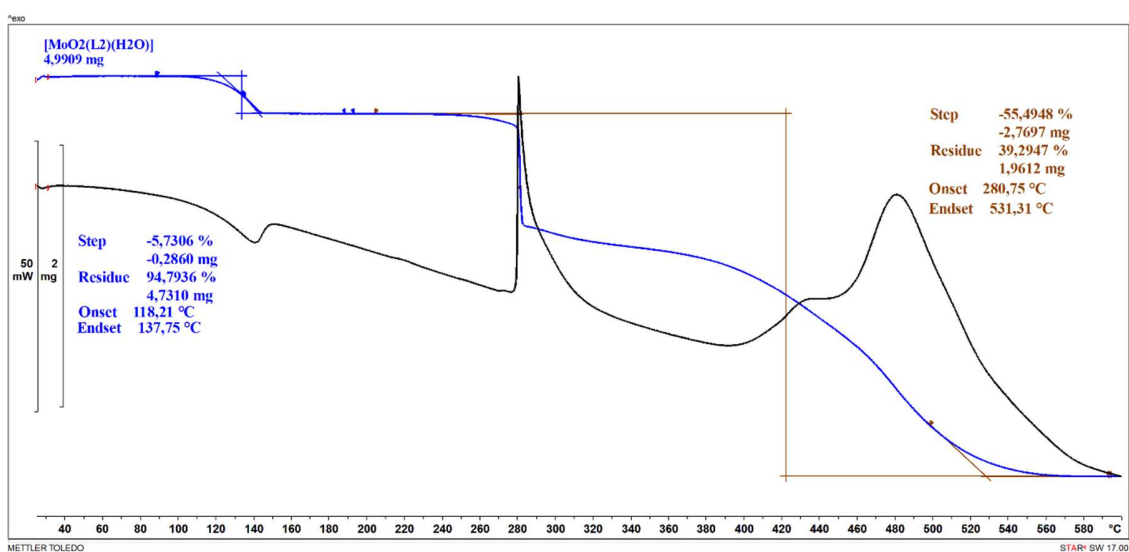


Figure S13. TGA/DSC curve for the complex [MoO₂(L²)(H₂O)] (3)

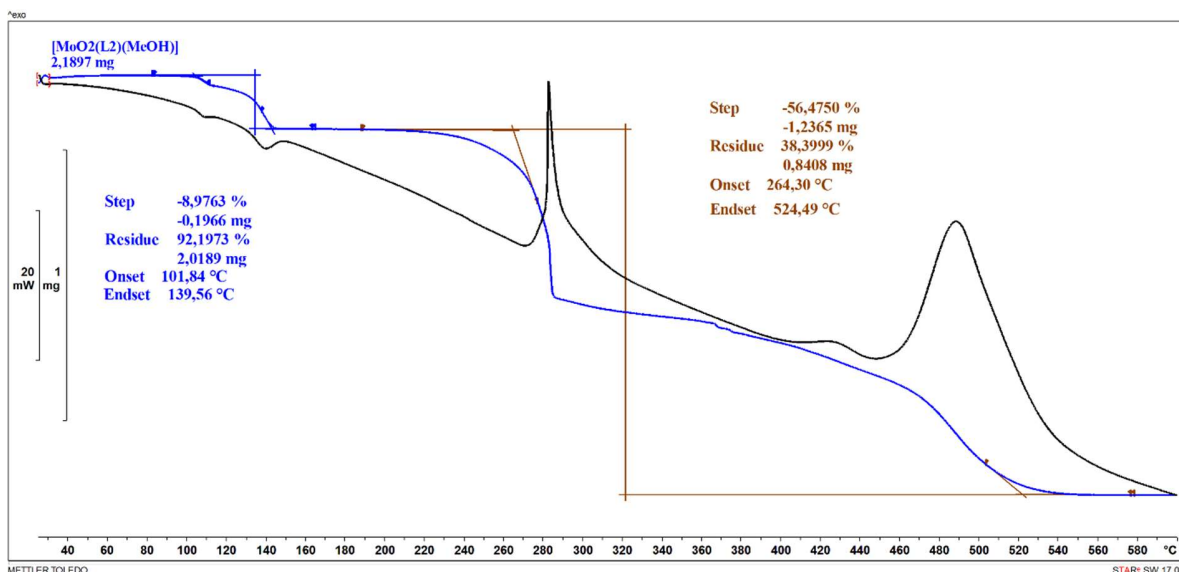


Figure S14. TGA/DSC curve for the complex [MoO₂(L²)(MeOH)] (4)

Synthesis of side product (pyH)₄Mo₈O₂₆

Ligand H₂L¹ (50.6 mg, 0.2604 mmol) was dissolved in 30 mL of acetonitrile in a 100 mL round bottom flask. Then 21 μL of pyridine and [MoO₂(acac)₂] (84.9 mg, 0.2604 mmol) were added. The reaction was refluxed for two hours and left until a precipitate appeared. The resulting blue-white crystals were analysed using IR-ATR spectroscopy and X-ray diffraction on a single crystal. Even though the mother solution was left for the evaporation, no expected pure compound (Mo complex) could be isolated even after prolonged standing.

Colour: while-blueish. Yield: 3%. IR-ATR: ν / cm⁻¹: 3216 ν N-H, 3070 ν C-H, 2962 ν C-H (CH₃), 2895 ν C-H (CH₂), 1605 i 1487 ν ring, 1529 ν C-N, 941, 897 i 649 ν O=Mo=O

Crystallographic data

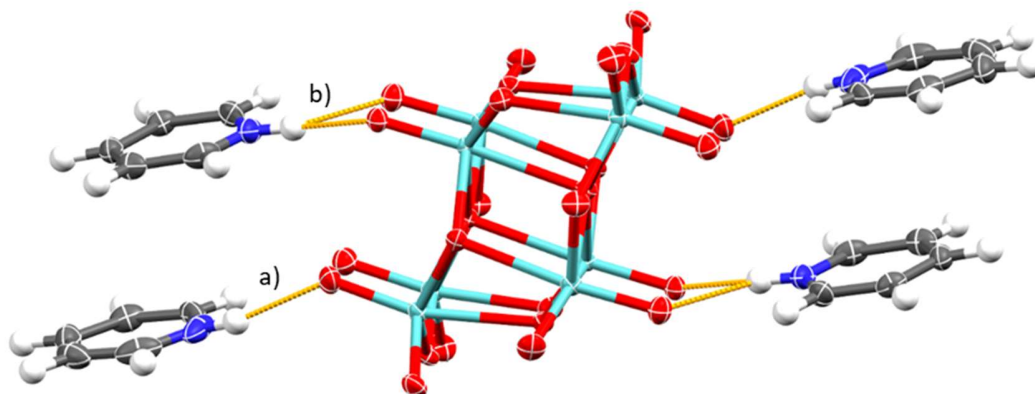
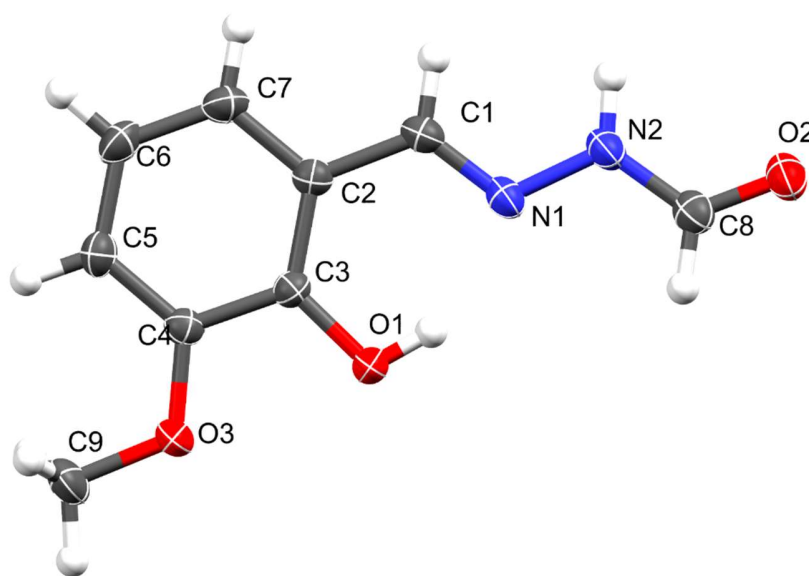
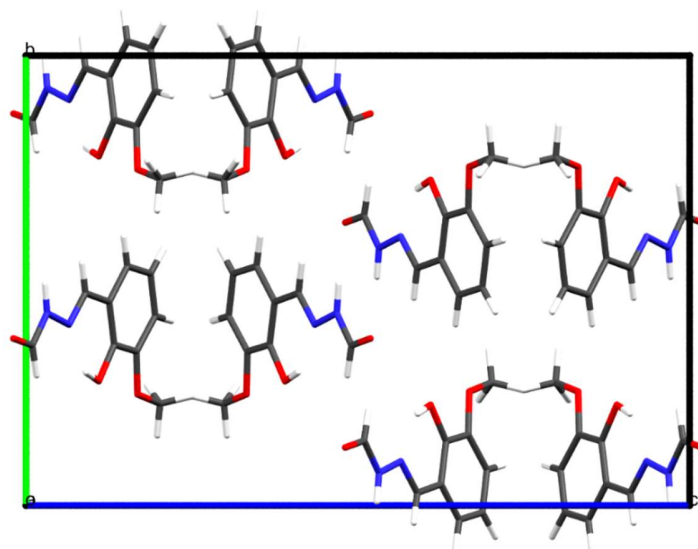


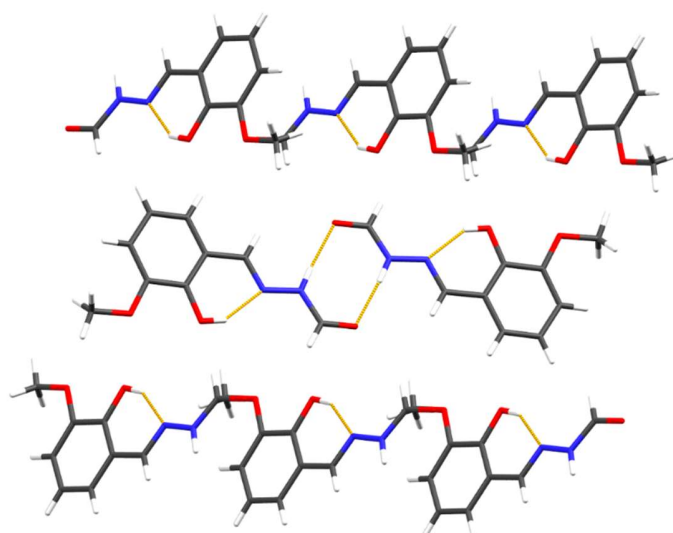
Figure S15. Supramolecular environment in the crystal structure of $(\text{pyH})_4(\text{Mo}_8\text{O}_{26})$. Pyridinium cations form a) normal and b) bifurcated hydrogen bonds with axial oxygen atoms of the octamolybdate anions. Atoms are shown as thermal ellipsoids with 50% probability.



(a)

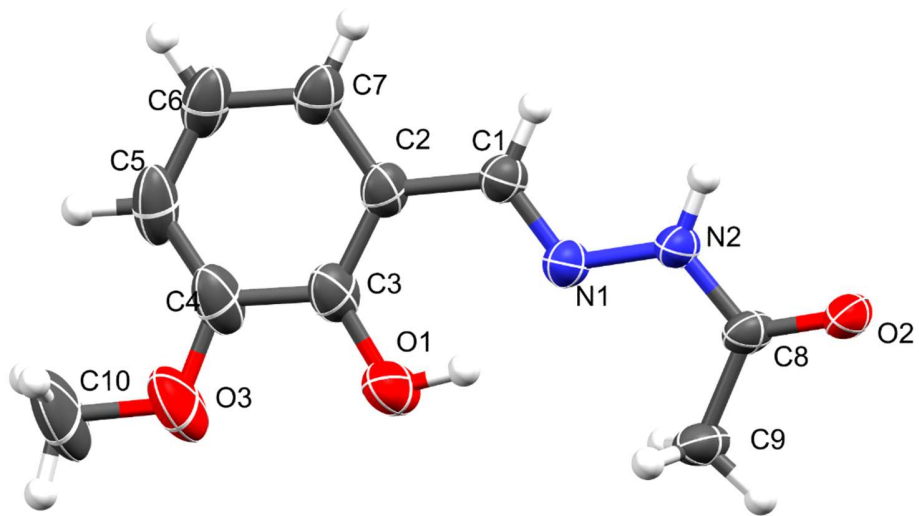


(b)

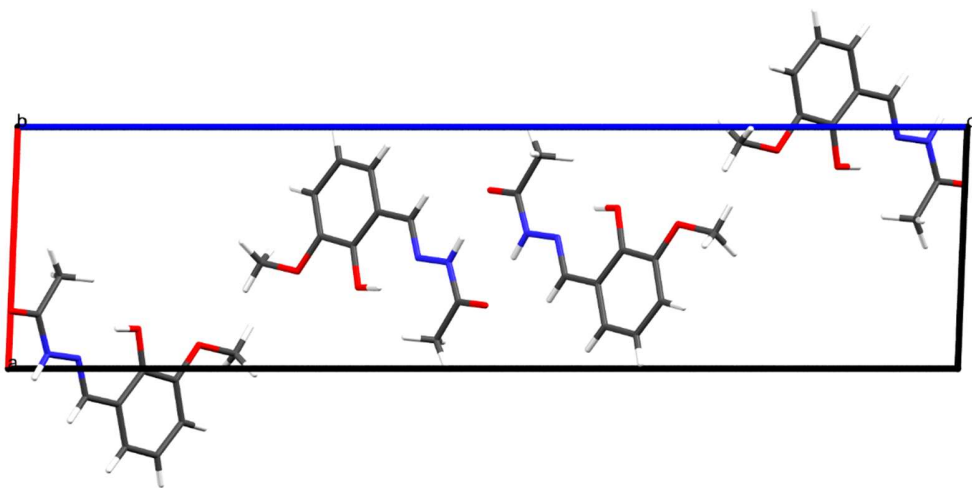


(c)

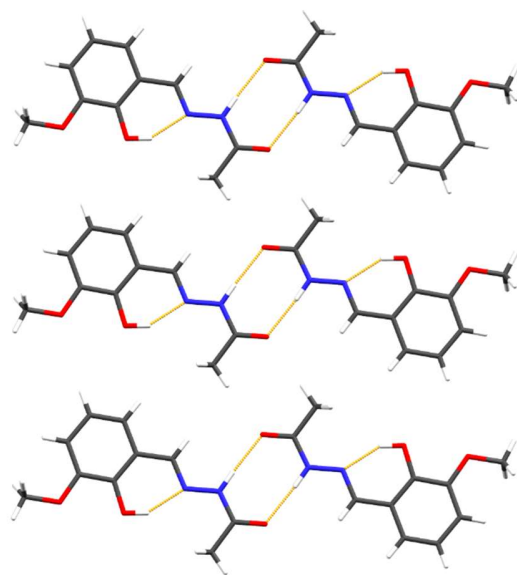
Figure S16. (a) Molecular structure of the ligand H_2L^1 . Atoms are shown as thermal ellipsoids with 50% probability. (b) Packing of molecules in the unit cell shown along a -axis. (c) Supramolecular homodimers of H_2L^1 are realized through amide (C=O)-NH synthon. The same are packed in zig-zag fashion.



(a)

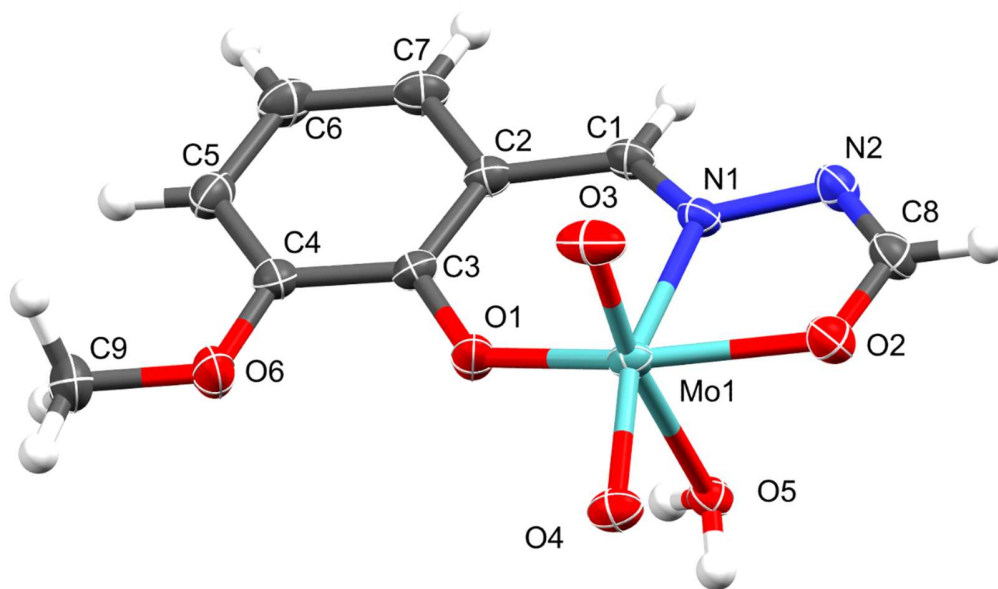


(b)

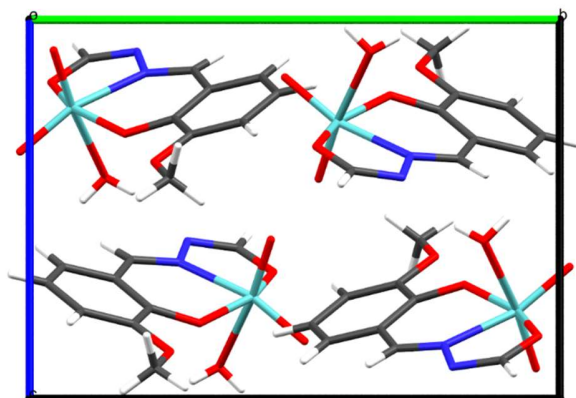


(c)

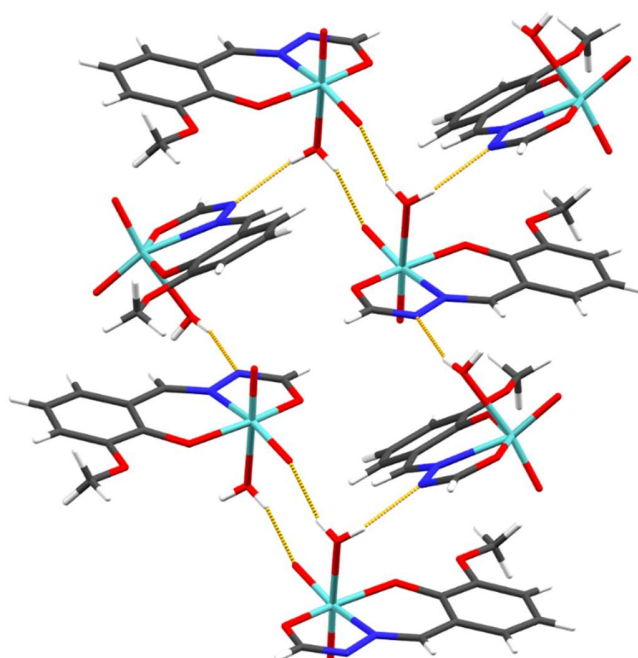
Figure S17. (a) Molecular structure of the ligand H_2L^2 . Atoms are shown as thermal ellipsoids with 50% probability. (b) Packing of molecules in the unit cell shown along b -axis. (c) As in H_2L^1 , supramolecular homodimers of H_2L^2 are realized through amide (C=O)-NH synthon. However, in this case the dimers form sheets *via* (C=O)-CH₃ short contacts.



(a)

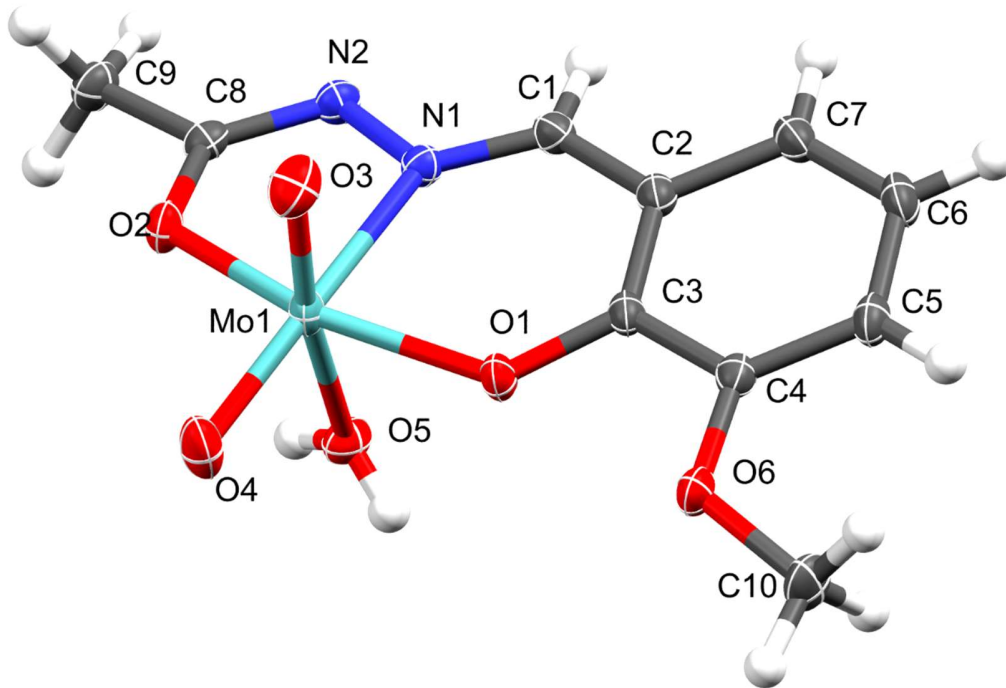


(b)

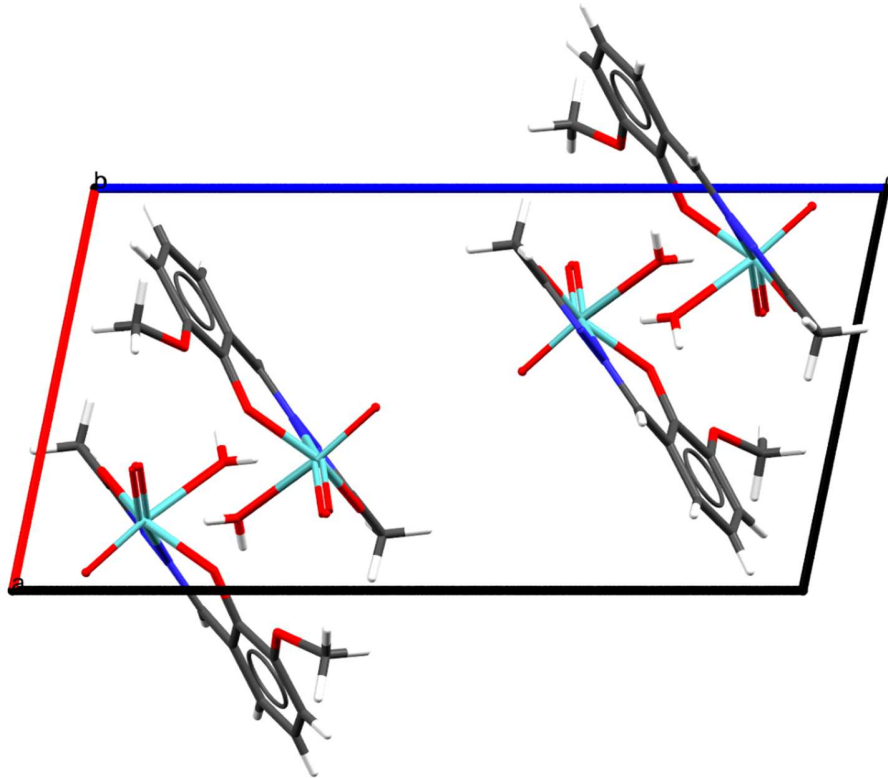


(c)

Figure S18. (a) Molecular structure of the complex $[\text{MoO}_2(\text{L}^1)(\text{H}_2\text{O})]$ (1). Atoms are shown as thermal ellipsoids with 50% probability. (b) Packing of molecules in the unit cell shown along a -axis. (c) The molecules of dioxomolybdenum(vi) complex show relatively complex supramolecular architecture, forming $R_6^c(24)$ and larger supramolecular rings through $\text{O}_w\text{-H}\cdots\text{O}=\text{Mo}$ and $\text{O}_w\text{-H}\cdots\text{N}_{\text{amide}}$ hydrogen bonds. The water ligand hydrogen bond donors not participating in the supramolecular ring structure interact with neighboring complex molecules by the same motifs, forming a supramolecular net.



(a)



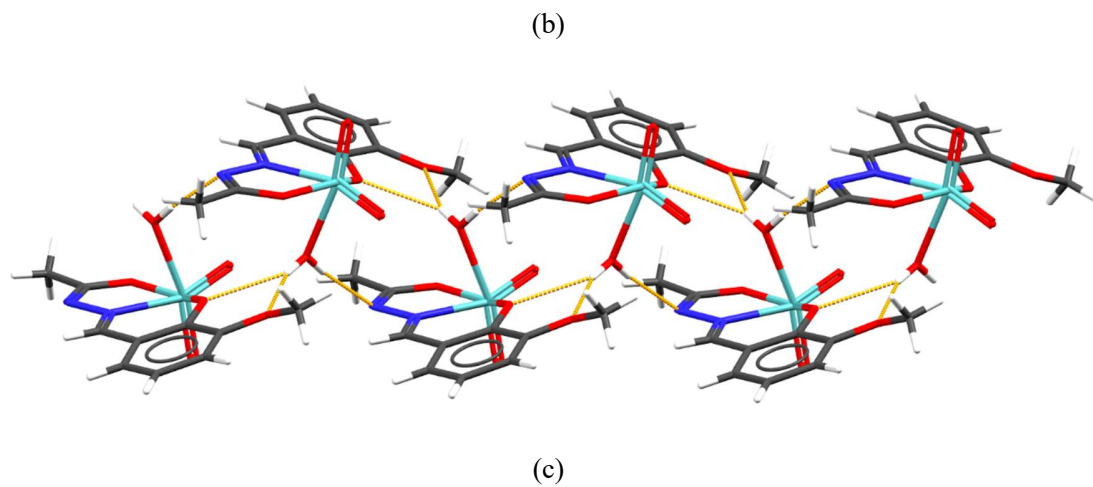
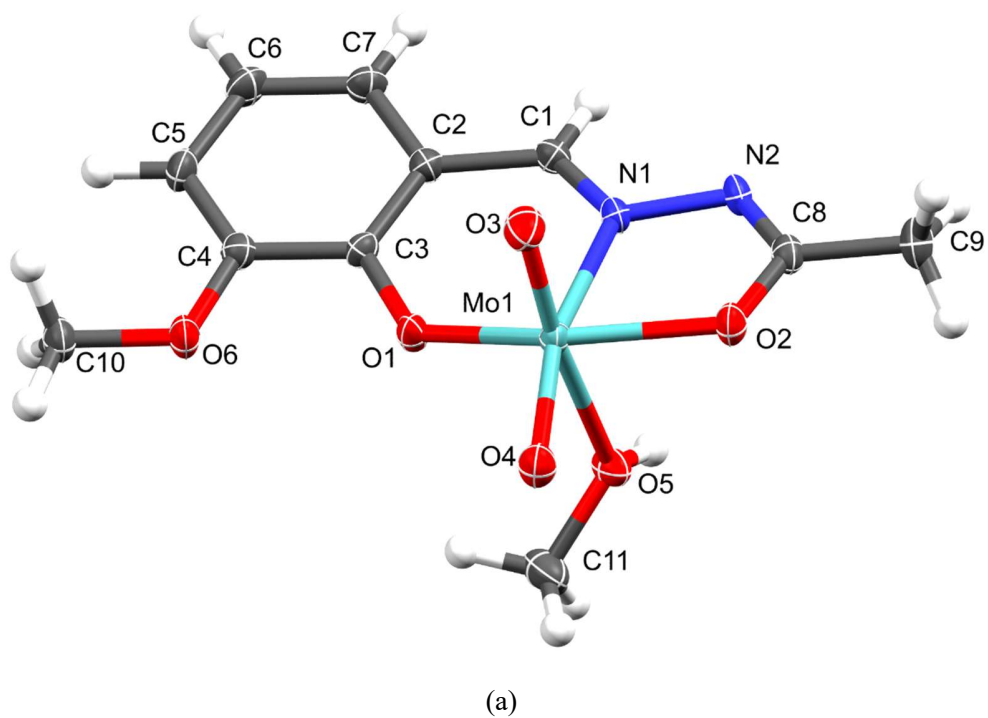
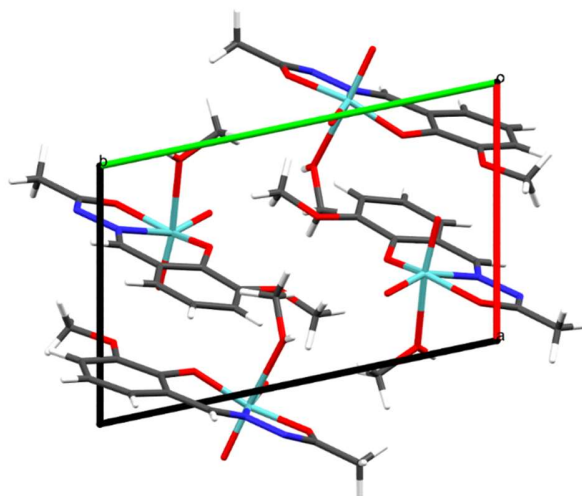
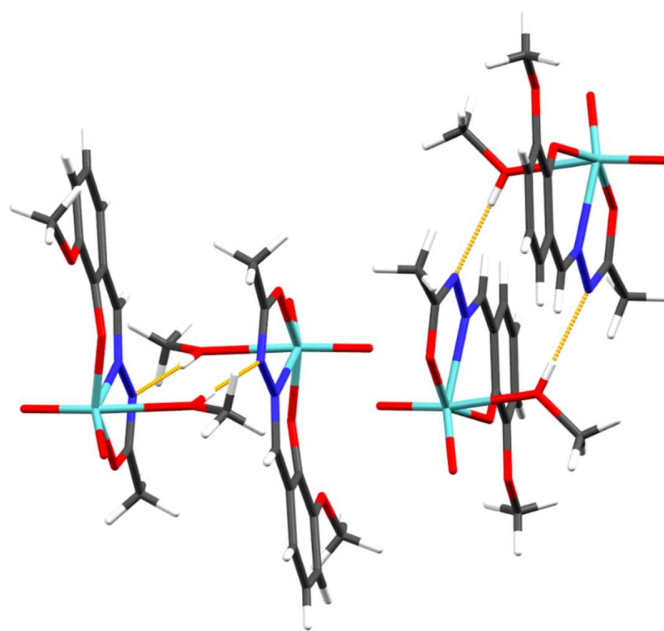


Figure S19. (a) Molecular structure of the complex $[\text{MoO}_2(\text{L}^2)(\text{H}_2\text{O})]$ (**3**). Atoms are shown as thermal ellipsoids with 50% probability. (b) Packing of molecules in the unit cell shown along b -axis. (c) Contrary to the L^1 counterpart, the molecules form supramolecular chains *via* $\text{O}_w\text{---H}\cdots\text{O}_{\text{phen}}$, $\text{O}_w\text{---H}\cdots\text{O}_{\text{methoxy}}$ and $\text{O}_w\text{---H}\cdots\text{N}_{\text{amide}}$ hydrogen bonds. The chains interact weakly through numerous $\text{Mo}=\text{O}_{\text{ax}}\cdots\text{H}\text{---}\text{C}$ contacts.





(b)



(c)

Figure S20. (a) Molecular structure of the complex $[\text{MoO}_2(\text{L}^2)(\text{MeOH})]$ (4). Atoms are shown as thermal ellipsoids with 50% probability. (b) Packing of molecules in the unit cell shown along c -axis. (c) Lacking a ditopical hydrogen bond donor, molecules of complex exclusively form non-interacting homodimers through $\text{O}_{\text{MeOH}}-\text{H}\cdots\text{N}_{\text{amide}}$ hydrogen bonds. Interestingly, the dimers form between symmetrically equivalent molecules, yielding two geometrically distinct (albeit very similar) dimer types. The dimers are bound with an assortment of weak $\text{C}-\text{H}\cdots\text{O}$ contacts.

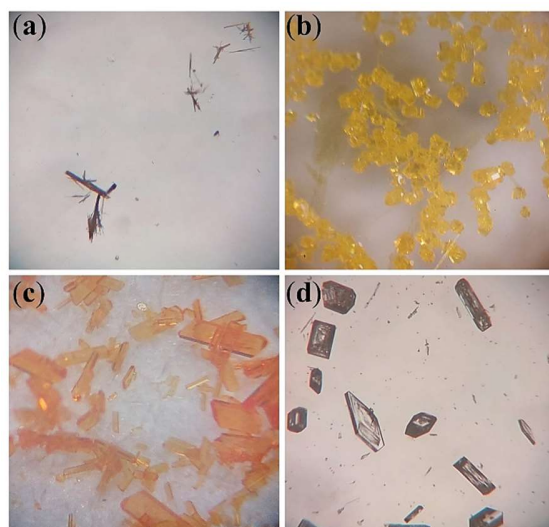


Figure S21. Photos of the single crystals analysed by SCXRD: (a) $[\text{MoO}_2(\text{L}^1)(\text{H}_2\text{O})]$, (b) $[\text{MoO}_2(\text{L}^2)(\text{H}_2\text{O})]$, (c) $[\text{MoO}_2(\text{L}^2)(\text{MeOH})]$, (d) $(\text{pyH})_4\text{Mo}_8\text{O}_{26}$

Table S1. Experimental and crystallographic data for crystal structures determined in this work.

Identifier	(pyH) ₄ (Mo ₈ O ₂₆)	H ₂ L ¹	H ₂ L ²	[MoO ₂ (L ¹)(H ₂ O)] (1)	[MoO ₂ (L ²)(H ₂ O)] (3)	[MoO ₂ (L ₂)(MeOH)] (4)
Empirical formula	C ₂₀ H ₂₄ Mo ₈ N ₄ O ₂₆	C ₉ H ₁₀ N ₂ O ₃	C ₁₀ H ₁₂ N ₂ O ₃	C ₉ H ₁₀ MoN ₂ O ₆	C ₁₀ H ₁₂ MoN ₂ O ₆	C ₁₁ H ₁₄ MoN ₂ O ₆
<i>M_r</i>	1503.95	194.19	208.22	338.13	352.16	366.18
<i>T</i> /K	171(2)	169.98(10)	169.99(10)	169.99(10)	169.99(10)	169.99(10)
Crystal system	triclinic, colourless irregular	orthorhombic, colourless plate	monoclinic, colourless needle	monoclinic, yellow plate	monoclinic, yellow prism	triclinic, orange plate
Space group	<i>P</i> −1	<i>Pbc</i> <i>a</i>	<i>P</i> 1 2 ₁ / <i>n</i> 1	<i>P</i> 1 2 ₁ / <i>c</i> 1	<i>P</i> 1 2 ₁ / <i>n</i> 1	<i>P</i> −1
<i>a</i> /Å	9.4160(5)	6.64651(4)	7.47100(10)	9.42370(10)	8.88447(5)	7.57710(10)
<i>b</i> /Å	9.9091(6)	13.62858(11)	4.59940(10)	13.18820(10)	8.26244(4)	12.47090(10)
<i>c</i> /Å	10.6597(7)	20.10991(17)	29.3867(5)	10.21520(10)	17.10001(10)	15.34390(10)
<i>α</i> /°	83.473(5)	90	90	90	90	72.3550(10)
<i>β</i> /°	76.788(5)	90	92.264(2)	112.7870(10)	101.6050(6)	88.6880(10)
<i>γ</i> /°	69.701(5)	90	90	90	90	78.2490(10)
<i>V</i> /Å ³	907.49(10)	1821.61(2)	1009.00(3)	1170.47(2)	1229.605(12)	1351.55(2)
<i>Z</i>	1	8	4	4	4	4
<i>ρ</i> _{calc} /g cm ^{−3}	2.752	1.416	1.371	1.919	1.902	1.800
<i>μ</i> /mm ^{−1}	22.833	0.911	0.858	9.427	9.003	8.218
<i>F</i> (000)	716	816	440	672	704	736

Crystal size/mm ³	0.17×0.06×0.02	0.1×0.08×0.02	0.1×0.01×0.01	0.04×0.03×0.01	0.15×0.07×0.03	0.1×0.05×0.02
Radiation	Cu Kα (λ = 1.54184Å)	Cu Kα (λ = 1.54184Å)	Cu Kα (λ = 1.54184Å)	Cu Kα (λ = 1.54184Å)	Cu Kα (λ = 1.54184Å)	Cu Kα (λ = 1.54184Å)
2θ range/°	8.526 to 156.254	8.794 to 155.544	6.02 to 155.028	10.182 to 155.57	10.47 to 155.36	6.05 to 155.41
Index ranges	-11 ≤ h ≤ 11, -12 ≤ k ≤ 12, -13 ≤ l ≤ 9	-6 ≤ h ≤ 8, -17 ≤ k ≤ 17, -25 ≤ l ≤ 25	-9 ≤ h ≤ 9, -5 ≤ k ≤ 5, -37 ≤ l ≤ 34	-11 ≤ h ≤ 11, -16 ≤ k ≤ 16, -12 ≤ l ≤ 12	-11 ≤ h ≤ 11, -9 ≤ k ≤ 10, -21 ≤ l ≤ 21	-9 ≤ h ≤ 9, -15 ≤ k ≤ 15, -18 ≤ l ≤ 19
Reflections collected	14478	34243	15152	40412	23467	24730
Independent reflections	3828 [R _{int} = 3.55%, R _{sigma} = 4.54 %]	1931 [R _{int} = 1.27%, R _{sigma} = 3.03 %]	2134 [R _{int} = 2.16%, R _{sigma} = 3.25 %]	2486 [R _{int} = 0.97%, R _{sigma} = 2.66 %]	2626 [R _{int} = 0.91%, R _{sigma} = 2.08 %]	5716 [R _{int} = 1.44%, R _{sigma} = 1.82 %]
Data/restraints/parameters	3828/-/269	1931/-/136	2134/-/146	2486/-/170	2626/-/180	5716/-/373
g ₁ , g ₂ in w ^a	0.0571, 0.3249	0.0416, 0.5245	0.0542, 0.2879	0.0238, 0.6892	0.0291, 0.9284	0.0271, 1.1723
Goodness-of-fit on F ² , S ^b	1.055	1.056	1.052	1.089	1.069	1.076
Final R and wR ^c values [I ≥ 2σ(I)]	R ₁ = 3.14%, wR ₂ = 8.6%	R ₁ = 3.14%, wR ₂ = 8.19%	R ₁ = 4.42%, wR ₂ = 11.13%	R ₁ = 1.58%, wR ₂ = 4.31%	R ₁ = 1.82%, wR ₂ = 4.91%	R ₁ = 2.0%, wR ₂ = 5.28%
Final R and wR ^c values [all data]	R ₁ = 3.25%, wR ₂ = 8.74%	R ₁ = 3.36%, wR ₂ = 8.27%	R ₁ = 5.14%, wR ₂ = 11.64%	R ₁ = 1.63%, wR ₂ = 4.34%	R ₁ = 1.83%, wR ₂ = 4.91%	R ₁ = 2.03%, wR ₂ = 5.3%
Largest diff. peak/hole / e Å ⁻³	0.864/-1.273	0.169/-0.201	0.150/-0.176	0.255/-0.469	0.280/-0.587	0.340/-0.577

$$^a w = 1/[\sigma F_o^2 + (g_1 P)^2 + g_2 P] \text{ where } P = (F_o^2 + 2F_c^2)/3$$

$$^b S = \{\Sigma[w(F_o^2 - F_c^2)2]/(N_r - N_p)\}^{1/2} \text{ where } N_r = \text{number of independent reflections, } N_p = \text{number of refined parameters.}$$

$$^c R = \Sigma||F_o| - |F_c||/\Sigma|F_o|; wR = \{\Sigma[w(F_o^2 - F_c^2)2]/\Sigma[w(F_o^2)2]\}^{1/2}$$

Table S2. Selected bond lengths in the determined crystal structures.

H₂L¹					
Atoms	Bond length/Å	Atoms	Bond length/Å	Atoms	Bond length/Å
C7–C2	1.4043(14)	C3–C4	1.4064(13)	O3–C4	1.3665(12)
C1–C6	1.3767(15)	O1–C3	1.3539(11)	O3–C9	1.4196(14)
C2–C3	1.4017(13)	O2–C8	1.2259(13)		
H₂L²					
Atoms	Bond length/Å	Atoms	Bond length/Å	Atoms	Bond length/Å
C2–C3	1.396(2)	C4–C5	1.377(3)	O3–C4	1.367(3)
C2–C7	1.407(2)	O1–C3	1.3554(19)	O3–C10	1.438(3)
C3–C4	1.406(2)	O2–C8	1.2376(18)		
[MoO₂(L¹)(H₂O)] (1)					
Atoms	Bond length/Å	Atoms	Bond length/Å	Atoms	Bond length/Å
C3–C4	1.405(3)	Mo1–O2	2.0149(14)	O1–C3	1.351(2)
C4–C5	1.386(2)	Mo1–O3	1.6876(13)	O2–C8	1.306(2)
C5–C6	1.395(3)	Mo1–O4	1.7200(11)	O6–C4	1.358(2)
C6–C7	1.372(3)	Mo1–O5	2.3563(12)	O6–C9	1.430(2)
Mo1–N1	2.2326(14)	N1–C1	1.289(2)		
Mo1–O1	1.9105(13)	N1–N2	1.409(2)		
[MoO₂(L²)(H₂O)] (3)					
Atoms	Bond length/Å	Atoms	Bond length/Å	Atoms	Bond length/Å
C3–C4	1.407(2)	Mo1–O2	2.0203(12)	O1–C3	1.346(2)
C4–C5	1.389(2)	Mo1–O3	1.6973(14)	O2–C8	1.308(2)
C5–C6	1.399(2)	Mo1–O4	1.7015(14)	O6–C4	1.366(2)
C6–C7	1.375(2)	Mo1–O5	2.3064(13)	O6–C10	1.439(2)
Mo1–N1	2.2458(14)	N1–C1	1.285(2)		
Mo1–O1	1.9426(12)	N1–N2	1.401(2)		
[MoO₂(L²)(MeOH)] (4)					
Atoms	Bond length/Å	Atoms	Bond length/Å	Atoms	Bond length/Å
C2–C7	1.409(3)	Mo1–O3	1.6974(15)	O1–C3	1.342(2)
C2A–C7A	1.409(3)	Mo1–O4	1.7030(14)	O1A–C3A	1.344(2)
C3–C4	1.408(3)	Mo1–O5	2.3414(15)	O2–C8	1.308(2)
C3A–C4A	1.408(3)	Mo1A–N1A	2.2389(15)	O2A–C8A	1.310(2)
C4–C5	1.382(3)	Mo1A–O1A	1.9185(14)	O5–C11	1.436(3)
C4A–C5A	1.388(3)	Mo1A–O2A	2.0253(14)	O5A–C11A	1.413(3)
C5–C6	1.399(3)	Mo1A–O3A	1.7004(15)	O6–C4	1.364(2)
C5A–C6A	1.396(3)	Mo1A–O4A	1.7036(14)	O6A–C4A	1.358(3)
Mo1–N1	2.2537(15)	Mo1A–O5A	2.3245(15)	O6–C10	1.424(3)
Mo1–O1	1.9314(14)	N1–N2	1.404(2)	O6A–C10A	1.425(3)
Mo1–O2	2.0202(14)	N1A–N2A	1.402(2)		

Table S3. Hydrogen bond parameters in the determined crystal structures.

H₂L¹					
D-H...A	D-H	H...A	D...A	∠D-H...A	Symmetry code
N2-H2...O2	0.893(15)	1.976(15)	2.8677(12)	176.0(12)	-x, 1-y, 1-z
C8-H1...O3	0.95	2.51	3.4103(12)	158	3/2-x, 1/2+y, z
H₂L²					
D-H...A	D-H	H...A	D...A	∠D-H...A	Symmetry code
N2-H2...O2	0.91(2)	1.93(2)	2.8416(15)	176.4(18)	1-x, -y, 1-z
C9-H9A...O2	0.98	2.45	3.4204(17)	171	2-x, -y, 1-z
C10-H10B...O3	0.98	2.58	3.510(3)	159	3/2-x, 1/2+y, 1/2-z
[MoO₂(L¹)(H₂O)] (1)					
D-H...A	D-H	H...A	D...A	∠D-H...A	Symmetry code
O5-H5A...N2	0.77(3)	2.05(3)	2.7965(18)	165(3)	x, 1/2-y, 1/2+z
O5-H5B...O4	0.79(3)	2.01(3)	2.7724(16)	164(3)	2-x, 1-y, 2-z
C5-H5...O3	0.95	2.54	3.408(2)	153	1-x, -1/2+y, 3/2-z
[MoO₂(L²)(H₂O)] (3)					
D-H...A	D-H	H...A	D...A	∠D-H...A	Symmetry code
O5-H5A...N2	0.78(3)	1.98(3)	2.749(2)	169(3)	1/2-x, 1/2+y, 3/2-z
O5-H5B...O1	0.80(3)	2.39(3)	3.0112(18)	136(2)	1/2-x, -1/2+y, 3/2-z
C7-H7...O3	0.95	2.59	3.358(2)	138	3/2-x, -1/2+y, 3/2-z
C10-H10C...O2	0.98	2.58	3.068(2)	110	1/2+x, 3/2-y, 1/2+z
[MoO₂(L²)(MeOH)] (4)					
D-H...A	D-H	H...A	D...A	∠D-H...A	Symmetry code
O5-H5...N2	0.79(3)	1.98(3)	2.773(2)	177(4)	-x, 1-y, -z
O5A-H5AA...N2A	0.77(4)	1.96(4)	2.734(2)	176(4)	2-x, -y, 1-z
C1-H1...O4A	0.95	2.42	3.294(2)	152	1-x, 1-y, -z
C1A-H1A...O3A	0.95	2.51	3.205(2)	130	1-x, -y, 1-z
C5A-H5AB...O4	0.95	2.49	3.212(3)	133	-x, 1-y, 1-z
C7-H7...O2A	0.95	2.52	3.371(2)	149	1-x, 1-y, -z
C9-H9A...O4A	0.98	2.46	3.330(3)	148	x, y, z
C10-H10C...O3A	0.98	2.51	3.420(3)	154	-1+x, 1+y, z

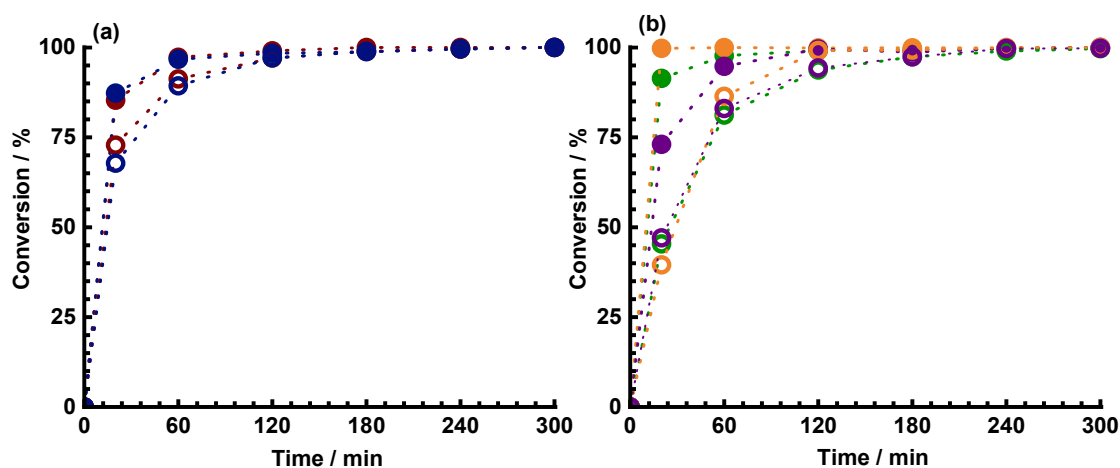


Figure S22. Kinetic profiles of linalool conversion with (a) $[\text{MoO}_2(\text{L}^1)]_n$ (2) and $[\text{MoO}_2(\text{L}^2)]_n$ (5) and (b) $[\text{MoO}_2(\text{L}^2)(\text{MeOH})]$ (4), $[\text{MoO}_2(\text{L}^1)(\text{H}_2\text{O})]$ (1) and $[\text{MoO}_2(\text{L}^2)(\text{H}_2\text{O})]$ (3). Solid circles represent reactions with TBHP in decane, while empty circles represent reactions with TBHP in water. Blue circles represent reactions with $[\text{MoO}_2(\text{L}^2)]_n$ (5), dark red circles with $[\text{MoO}_2(\text{L}^1)]_n$ (2), orange circles with $[\text{MoO}_2(\text{L}^2)(\text{H}_2\text{O})]$ (3), green circles with $[\text{MoO}_2(\text{L}^1)(\text{H}_2\text{O})]$ (1), and purple circles with $[\text{MoO}_2(\text{L}^2)(\text{MeOH})]$ (4).

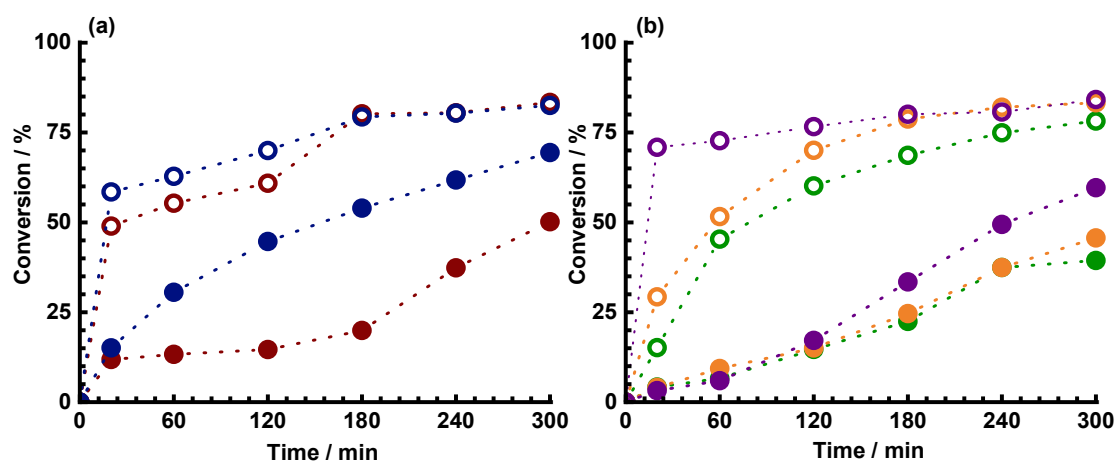


Figure S23. Kinetic profiles of linalool conversion with (a) $[\text{MoO}_2(\text{L}^1)]_n$ (2) and $[\text{MoO}_2(\text{L}^2)]_n$ (5) and (b) $[\text{MoO}_2(\text{L}^2)(\text{MeOH})]$ (4), $[\text{MoO}_2(\text{L}^1)(\text{H}_2\text{O})]$ (1) and $[\text{MoO}_2(\text{L}^2)(\text{H}_2\text{O})]$ (3). Solid circles represent reactions with H₂O₂, while empty circles represent reactions with H₂O₂ with acetonitrile. Blue circles represent reactions with $[\text{MoO}_2(\text{L}^2)]_n$ (5), dark red circles with $[\text{MoO}_2(\text{L}^1)]_n$ (2), orange circles with $[\text{MoO}_2(\text{L}^2)(\text{H}_2\text{O})]$ (3), green circles with $[\text{MoO}_2(\text{L}^1)(\text{H}_2\text{O})]$ (1), and purple circles with $[\text{MoO}_2(\text{L}^2)(\text{MeOH})]$ (4).

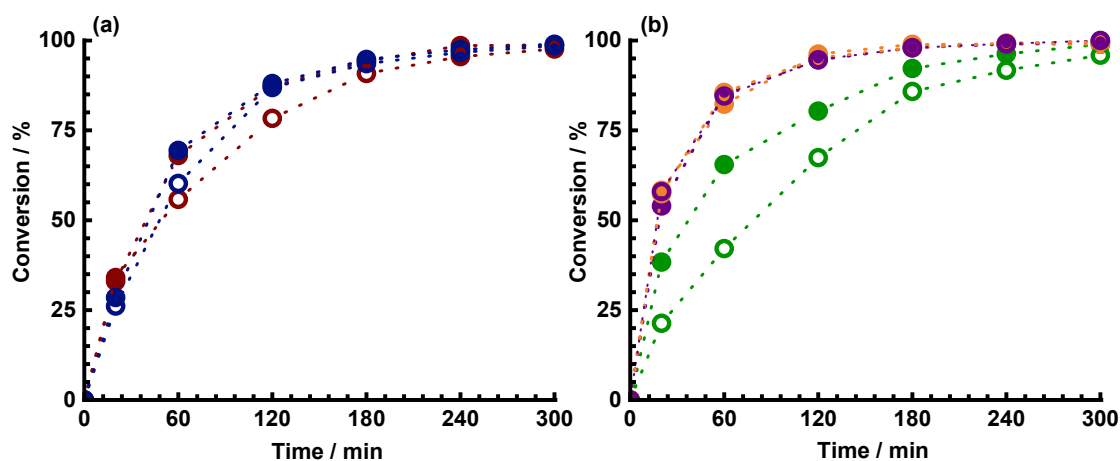


Figure S24. Kinetic profiles of linalool conversion with (a) $[\text{VO}_2(\text{HL}^{1*})]$ and $[\text{VO}_2(\text{HL}^{2*})]$ and (b) $[\text{VO}(\text{L}^{1*})(\text{OMe})(\text{MeOH})]$, $[\text{VO}(\text{L}^2)(\text{OEt})(\text{H}_2\text{O})]$, and $[\text{VO}(\text{L}^2)(\text{OMe})(\text{MeOH})]$. Solid circles represent reactions with TBHP in decane, while empty circles represent reactions with TBHP in water. Dark red circles represent reactions with $[\text{VO}_2(\text{HL}^{1*})]$, blue circles with $[\text{VO}_2(\text{HL}^{2*})]$, green circles with $[\text{VO}(\text{L}^{1*})(\text{OMe})(\text{MeOH})]$, orange circles with $[\text{VO}(\text{L}^2)(\text{OEt})(\text{H}_2\text{O})]$, and purple circles with $[\text{VO}(\text{L}^2)(\text{OMe})(\text{MeOH})]$.

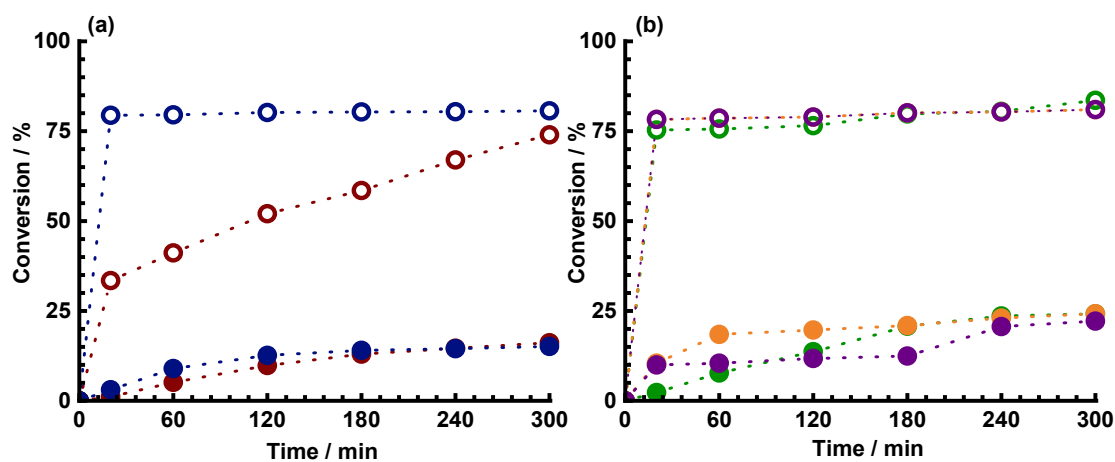


Figure S25. Kinetic profiles of linalool conversion with (a) $[\text{VO}_2(\text{HL}^{1*})]$ and $[\text{VO}_2(\text{HL}^{2*})]$ and (b) $[\text{VO}(\text{L}^{1*})(\text{OMe})(\text{MeOH})]$, $[\text{VO}(\text{L}^2)(\text{OEt})(\text{H}_2\text{O})]$, and $[\text{VO}(\text{L}^2)(\text{OMe})(\text{MeOH})]$. Solid circles represent reactions with H_2O_2 , while empty circles represent reactions with H_2O_2 with the addition of acetonitrile. Dark red circles represent reactions with $[\text{VO}_2(\text{HL}^{1*})]$, blue circles with $[\text{VO}_2(\text{HL}^{2*})]$, green circles with $[\text{VO}(\text{L}^{1*})(\text{OMe})(\text{MeOH})]$, orange circles with $[\text{VO}(\text{L}^2)(\text{OEt})(\text{H}_2\text{O})]$, and purple circles with $[\text{VO}(\text{L}^2)(\text{OMe})(\text{MeOH})]$.

Table S4. Catalytic results of linalool oxidation with vanadium catalysts. The reaction was carried out at 80 °C with TBHP in decane and TBHP in water, and at 70 °C with H₂O₂. $n(\text{catalyst})/n(\text{linalool})/n(\text{oxidant}) = 0.05 \text{ mmol}/10 \text{ mmol}/20 \text{ mmol}$.

CATALYST	Conversion ^a /%		TOF _{20min} ^b		TON ^c		Furanoid yield/%		Pyranoid yield/%	
	TBHPdec	TBHPaq	TBHPdec	TBHPaq	TBHPdec	TBHPaq	TBHPdec	TBHPaq	TBHPdec	TBHPaq
(NH ₄)[VO ₂ (L ^{1*})]	> 99	> 98	200	207	197	195	17	19	4	10
[VO ₂ (HL ^{2*})]			174	159	198	197	12	23	2	17
[VO(L ^{1*})(OMe)(MeOH)]			232	131	198	192	25	19	8	11
	H₂O₂	H₂O₂ MeCN	H₂O₂	H₂O₂+ MeCN	H₂O₂	H₂O₂+ MeCN	H₂O₂	H₂O₂+ MeCN	H₂O₂	H₂O₂+ MeCN
(NH ₄)[VO ₂ (L ^{1*})]	16	74	7	200	32	148	6	18	4	11
[VO ₂ (HL ^{2*})]	15	81	18	476	30	161	6	30	3	17
[VO(L ^{1*})(OMe)(MeOH)]	24	84	14	451	48	167	7	29	4	20

^a linalool consumed at the end of reaction. ^b $n(\text{linalool})$ transformed/ $n(\text{catalyst})$ /time(h) at 20 min. ^c $n(\text{linalool})$ transformed/ $n(\text{catalyst})$ at the end of reaction.

*TBHP stands for tert-butyl hydroperoxide, H₂O₂ for hydrogen peroxide, MeCN acetonitrile, dec for decane and aq for aqueous.

Catalytic results and discussion for the vanadium catalysts

The previously reported and characterized vanadium complexes $(\text{NH}_4)[\text{VO}_2(\text{L}^1^*)]$, $[\text{VO}_2(\text{HL}^{2*})]$, $[\text{VO}(\text{L}^1^*)(\text{OMe})(\text{MeOH})]$, $[\text{VO}(\text{L}^2)(\text{OEt})(\text{H}_2\text{O})]$, and $[\text{VO}(\text{L}^2)(\text{OMe})(\text{MeOH})]$ were evaluated as catalysts for the oxidation of linalool. Various oxidizing agents, including TBHP (in decane or in water) and H_2O_2 (with or without addition of the acetonitrile), were utilized. The results are summarized in Tables 3 and S4.

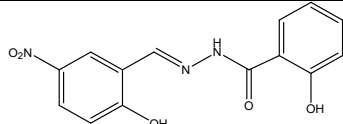
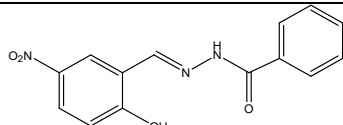
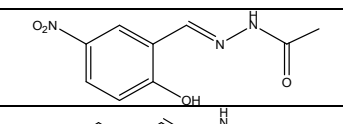
For these vanadium catalysts, the use of TBHP in either decane or water did not significantly affect the maximum linalool conversion rates, which were consistently above 98 %. The only exception was $[\text{VO}(\text{L}^1^*)(\text{OMe})(\text{MeOH})]$ which achieved a slightly lower conversion rate of 96 %. However, the use of H_2O_2 with or without the addition of acetonitrile, tremendously affected the maximum conversion rates. When acetonitrile was added, the conversion rates ranged from 74 % to 84 %, whereas without acetonitrile, the conversion rates were substantially lower, 15-24 %. The highest furanoid yields were obtained using H_2O_2 with the addition of acetonitrile, ranging from 18 % to 30 %, with $[\text{VO}_2(\text{HL}^{2*})]$ achieving the highest yield. The use of TBHP in decane or water resulted in similar furanoid yields, 12-25 %, which were generally higher than those obtained using H_2O_2 alone, cca 6 %. The lowest furanoid yields and conversion rates were observed when using H_2O_2 without acetonitrile, for the catalysts $(\text{NH}_4)[\text{VO}_2(\text{L}^1^*)]$ and $[\text{VO}_2(\text{HL}^{2*})]$. Regarding pyranoid yields, similar results were observed when TBHP in decane and H_2O_2 were used, with yields ranging from 2 % to 8 %. When TBHP in water and H_2O_2 with acetonitrile were used, the pyranoid yields improved significantly ranging from 10 % to 33 %. The highest pyranoid yield, 33%, was achieved with $[\text{VO}(\text{L}^2)(\text{OEt})(\text{H}_2\text{O})]$ as the catalyst.

The $\text{TOF}_{20\text{min}}$ values for TBHP were similar across most catalysts, except for $[\text{VO}(\text{L}^1^*)(\text{OMe})(\text{MeOH})]$, where the TOF value increased by 100 when TBHP in decane was used, resulting in a TOF of 232. The lowest TOF values were observed when H_2O_2 as oxidant was used. Adding acetonitrile to the reaction mixture significantly impacted the TOF values for two catalysts, increasing them by 26 and 32 times, respectively. For $[\text{VO}_2(\text{HL}^{2*})]$, the TOF increased from 18 to 476, the highest TOF value among the vanadium catalysts tested in this study, while for $[\text{VO}(\text{L}^1^*)(\text{OMe})(\text{MeOH})]$, the TOF increased to 451. Turnover number (TON) values were consistently in the range from 192 to 200 when TBHP was used, which is the maximum value observed. The TON values were the lowest with H_2O_2 alone, but the addition of acetonitrile increased them by 3 to 5 times.

In comparison to previously published results²², which utilized a vanadium loading of 0.25 % under identical reaction conditions, the primary difference lies in the use of a dinuclear catalyst $[\text{VO}(\text{SAP})]_2\text{O}$ in the reported research, whereas in this study only mononuclear vanadium catalysts were explored. The use of TBHP in either decane or water yielded comparable conversion results. When H_2O_2 was used, with or without the addition of acetonitrile, higher conversion rates were achieved than with the catalysts employed in this study. In all cases, conversion rates were above 90 % for $[\text{VO}(\text{SAP})]_2\text{O}$. For furanoid yield, the highest yield of 38 % was obtained with the $[\text{VO}(\text{SAP})]_2\text{O}$ catalyst using TBHP in decane as the oxidant. Similar yields were observed with other oxidants compared to the catalyst used in this research. For pyranoid yield, the best result of 33 % was achieved with $[\text{VO}(\text{L}^2)(\text{OEt})(\text{H}_2\text{O})]$ using H_2O_2 with the addition of acetonitrile, compared to a yield of 19 % when $[\text{VO}(\text{SAP})]_2\text{O}$ was used. The yields with other oxidants were quite similar.

Electrical characterisation of previously reported Mo and V complexes

Table S5. Activation energy values for the DC conductivity in the cooling cycle of the prepared complexes. DC conductivity values for all compounds measured @200 °C in the cooling run.

Compounds	$E_{DC}/\text{kJ mol}^{-1}$ (Cooling Run)	$\sigma_{DC}/(\Omega \text{ cm})^{-1}$	Reference	Ligand
$[\text{MoO}_2(\text{L}^1)(\text{MeOH})]$	65	1.82×10^{-9}	Sarjanović Materials	
$[\text{MoO}_2(\text{L}^1)]_n$	67	3.35×10^{-10}		
$[\text{MoO}_2(\text{L}^2)(\text{MeOH})]$	66	1.52×10^{-14}		
$[\text{MoO}_2(\text{L}^2)(\text{H}_2\text{O})]$	105	3.43×10^{-13}		
$[\text{MoO}_2(\text{L})(\text{MeOH})]$	60	2.8×10^{-14}	Šušković IJMS	
$[\text{MoO}_2(\text{L})(\text{H}_2\text{O})]$	102	1.0×10^{-12}		
$(\text{NH}_4)[\text{VO}_2(\text{L}^{1*})]$	54	2.6×10^{-9}	Sarjanović IJMC C	
$[\text{VO}(\text{L}^{1*})(\text{OMe})(\text{MeOH})]$	54	2.2×10^{-10}		
$[\text{VO}_2(\text{HL}^{2*})]$	75	1.2×10^{-9}		
$[\text{VO}(\text{L}^2)(\text{OMe})(\text{MeOH})]$ (complex 6)	67	7.0×10^{-10}		
$[\text{VO}_2(\text{HL}^2)]_2 \cdot 2\text{H}_2\text{O}$ (complex 7)	68	5.7×10^{-11}		

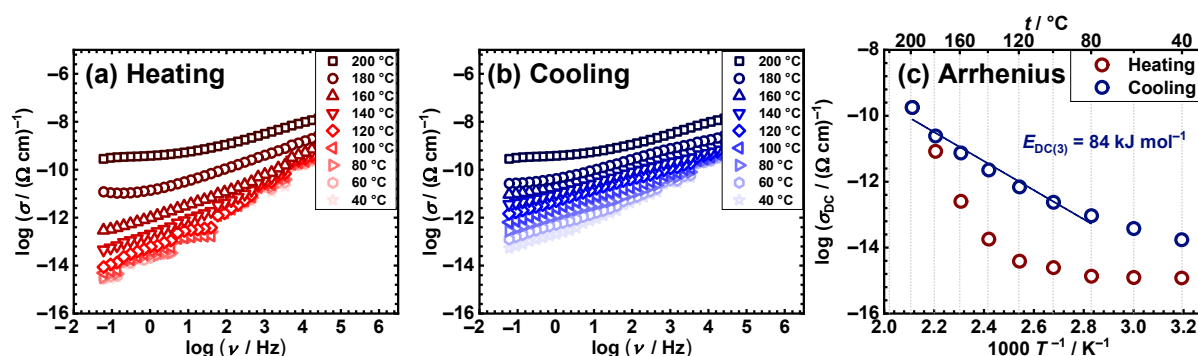


Figure S26. Conductivity spectra for mononuclear $[\text{MoO}_2(\text{L}^2)(\text{H}_2\text{O})]$ (3) compound in heating (a) and cooling (b) runs, along with (c) Arrhenius plots for DC conductivity for both runs (red circle – heating, blue circle – cooling).

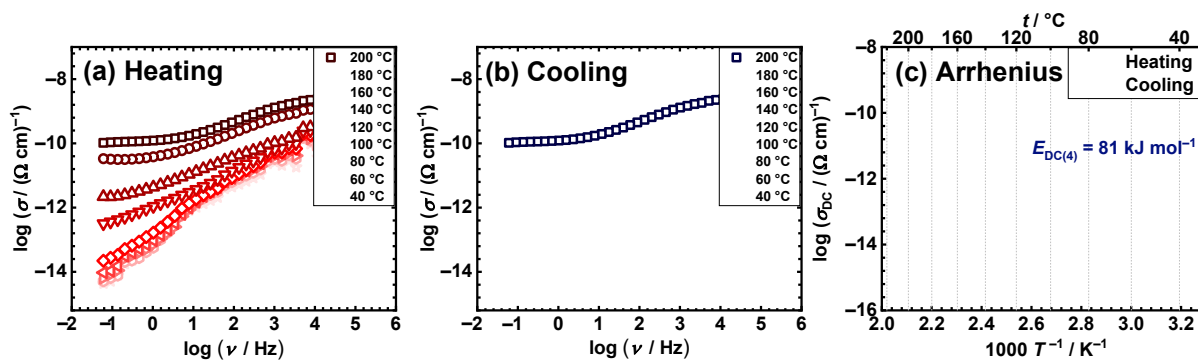
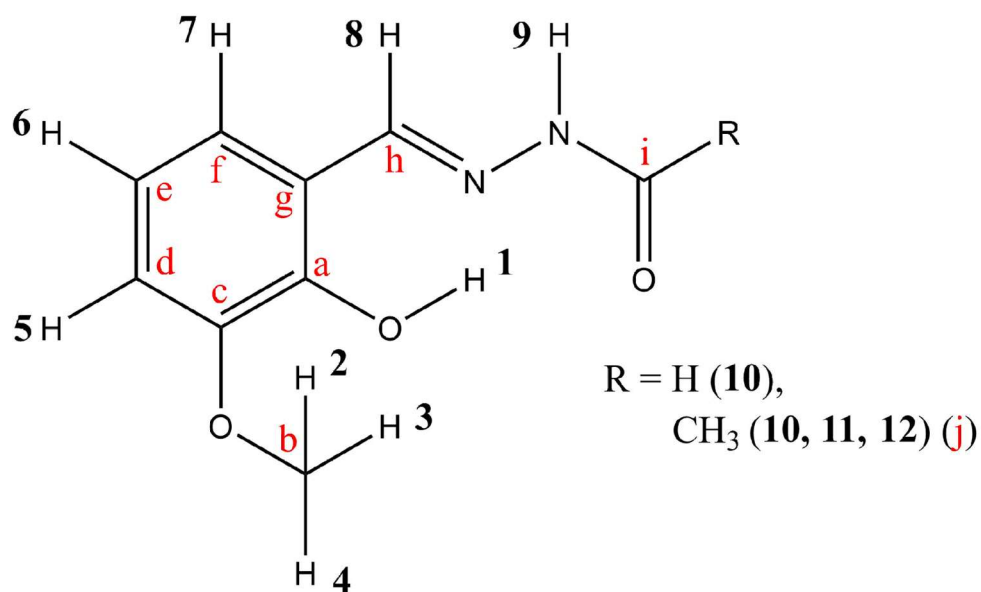


Figure S27. Conductivity spectra for mononuclear $[\text{MoO}_2(\text{L}^2)(\text{MeOH})]$ (4) compound in heating (a) and cooling (b) runs, along with (c) Arrhenius plots for DC conductivity for both runs (red circle – heating, blue circle – cooling).



Scheme S2. Structural representation of ligands H_2L^1 and H_2L^2 with NMR labels

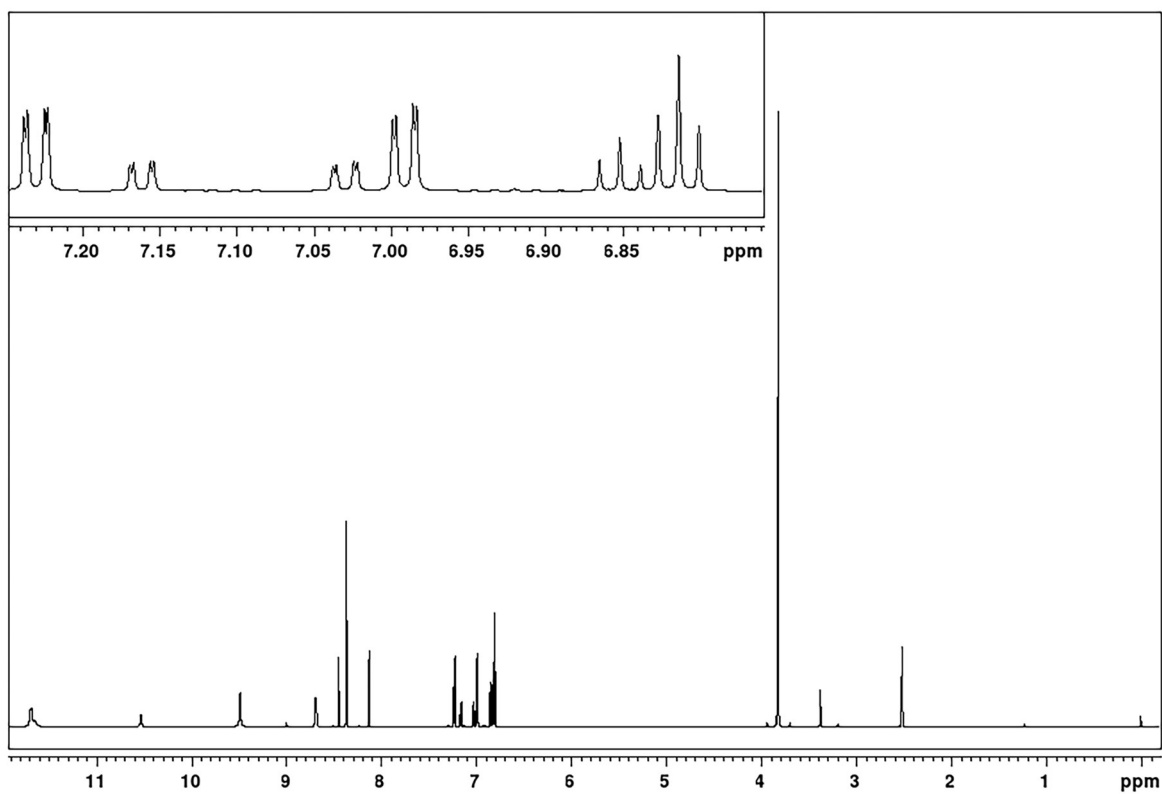


Figure S28. ^1H NMR spectrum of the ligand H_2L^1 with an enlarged view of the signals at chemical shifts from 6.77 to 7.42 ppm

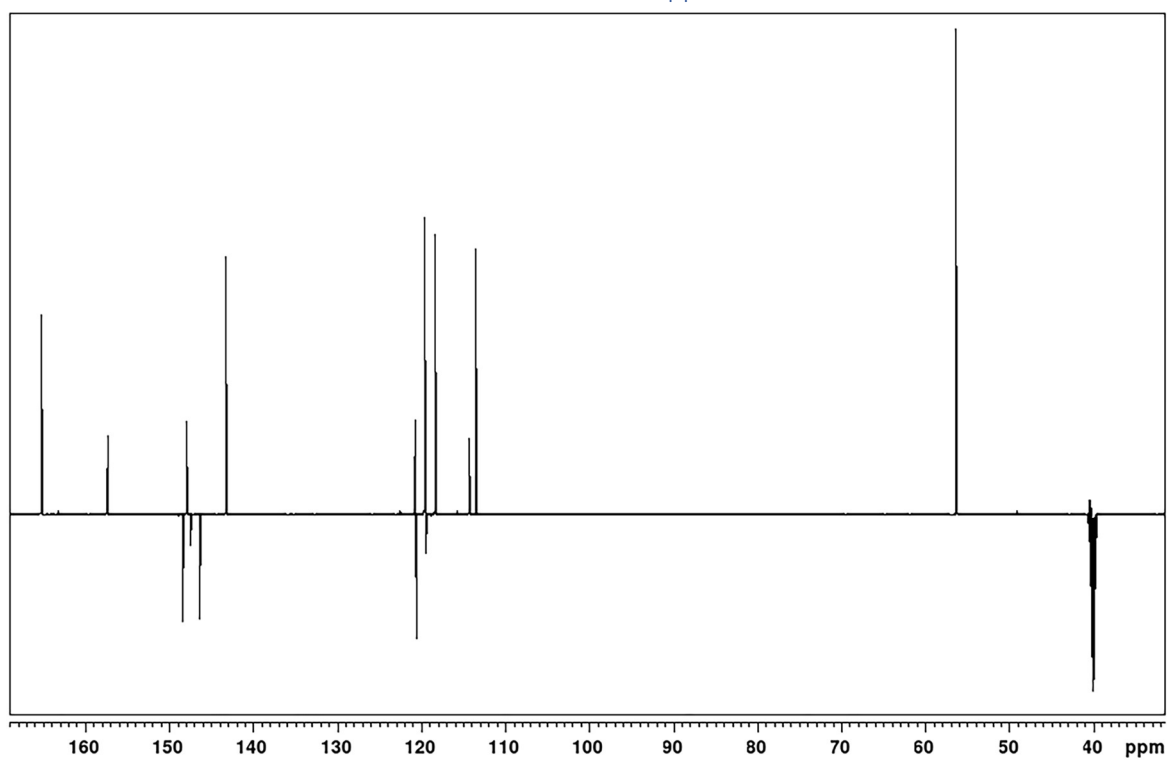


Figure S29. ^{13}C NMR spectra of the ligand H_2L^1

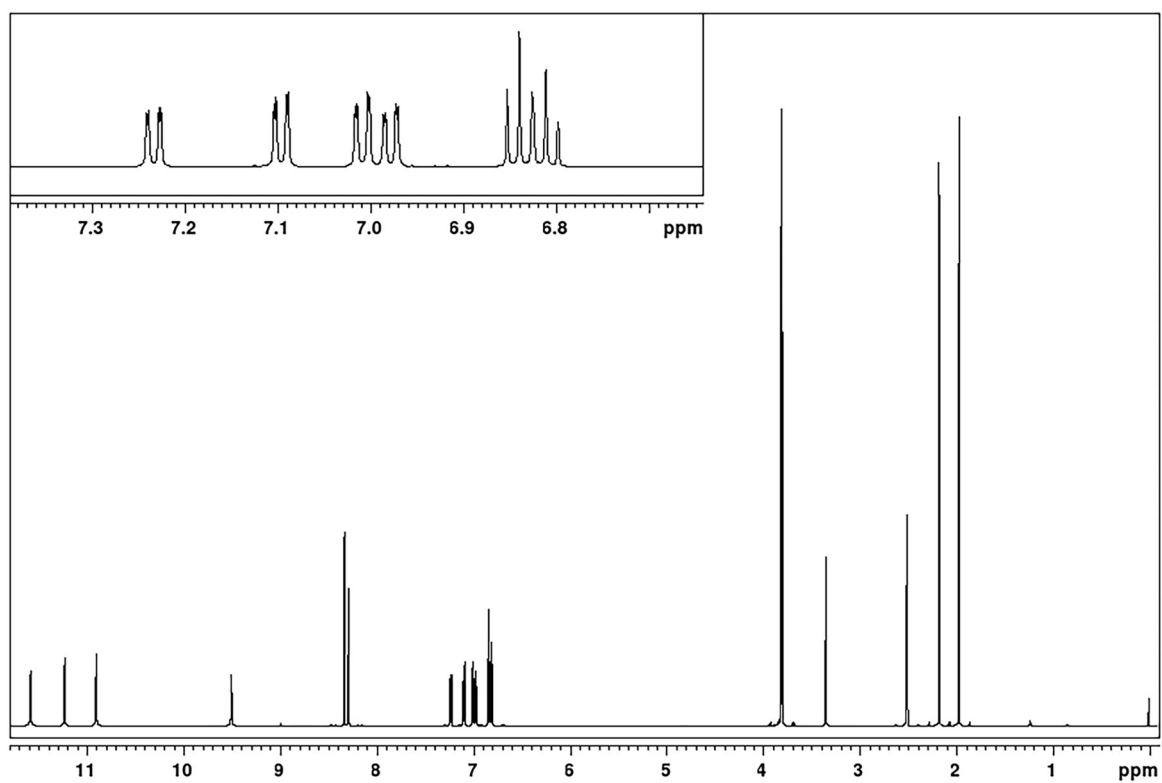


Figure S30. ^1H NMR spectrum of the ligand H_2L^2 with an enlarged view of the signals at chemical shifts from 6.70 to 7.30 ppm

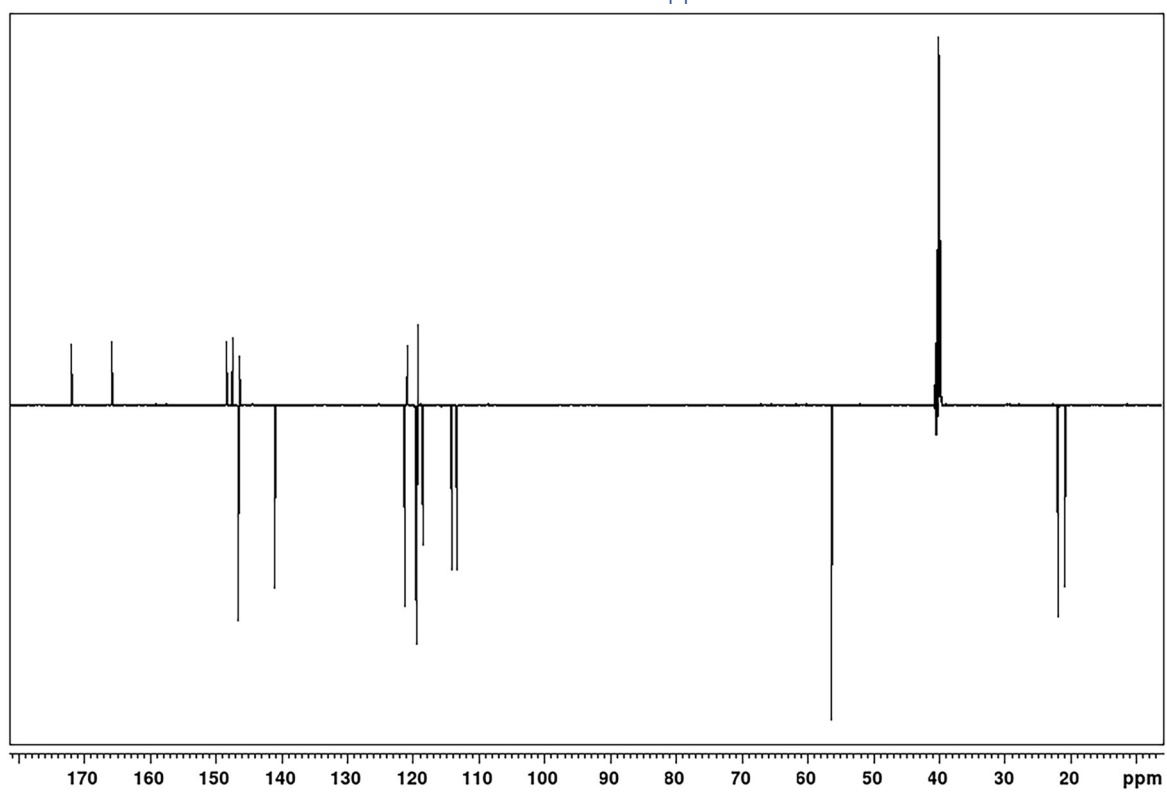
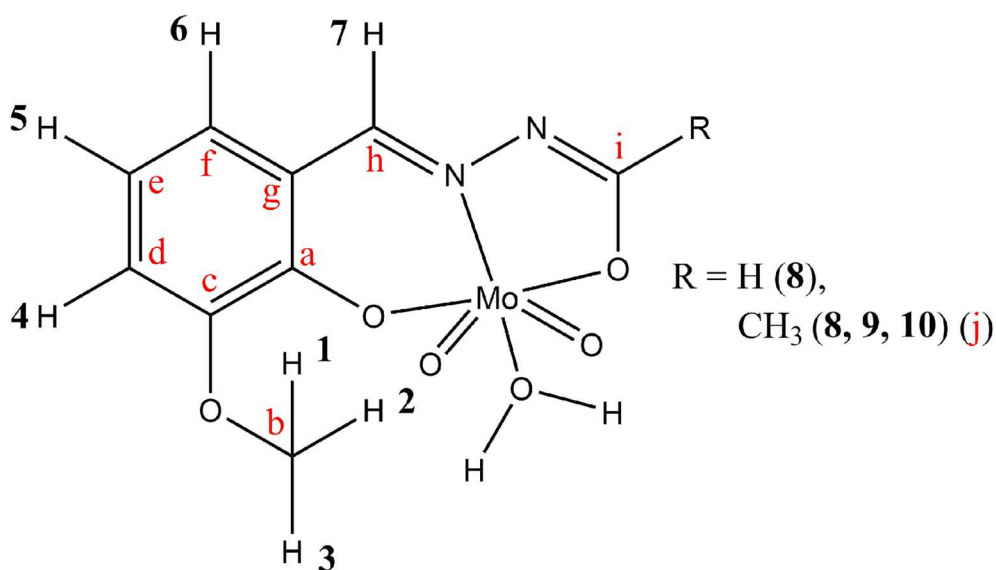


Figure S31. ^{13}C NMR spectra of the ligand H_2L^2



Scheme S3. Structural representation of the complexes $[\text{MoO}_2(\text{L}^1)(\text{H}_2\text{O})]$ (1) and $[\text{MoO}_2(\text{L}^2)(\text{H}_2\text{O})]$ (3) with NMR labels

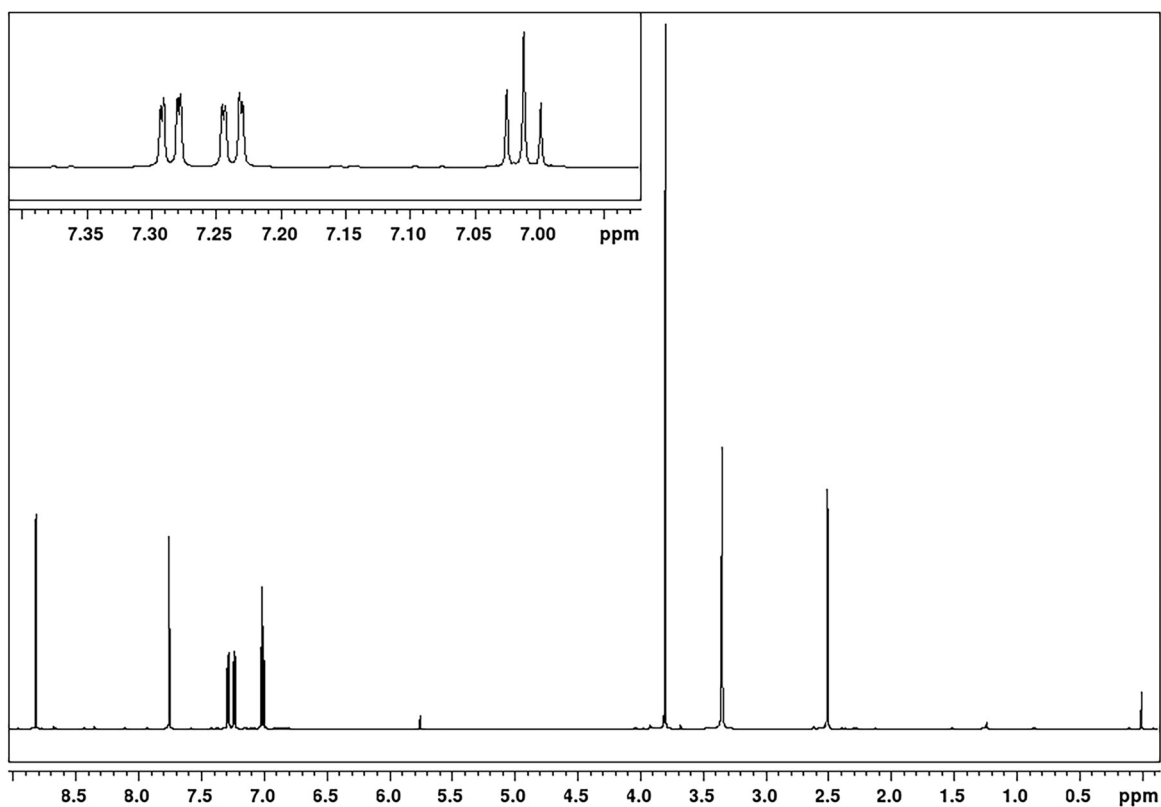


Figure S32. ^1H NMR spectrum of the complex $[\text{MoO}_2(\text{L}^1)(\text{H}_2\text{O})]$ (1) with an enlarged view of the signals at chemical shifts from 6.90 to 7.35 ppm

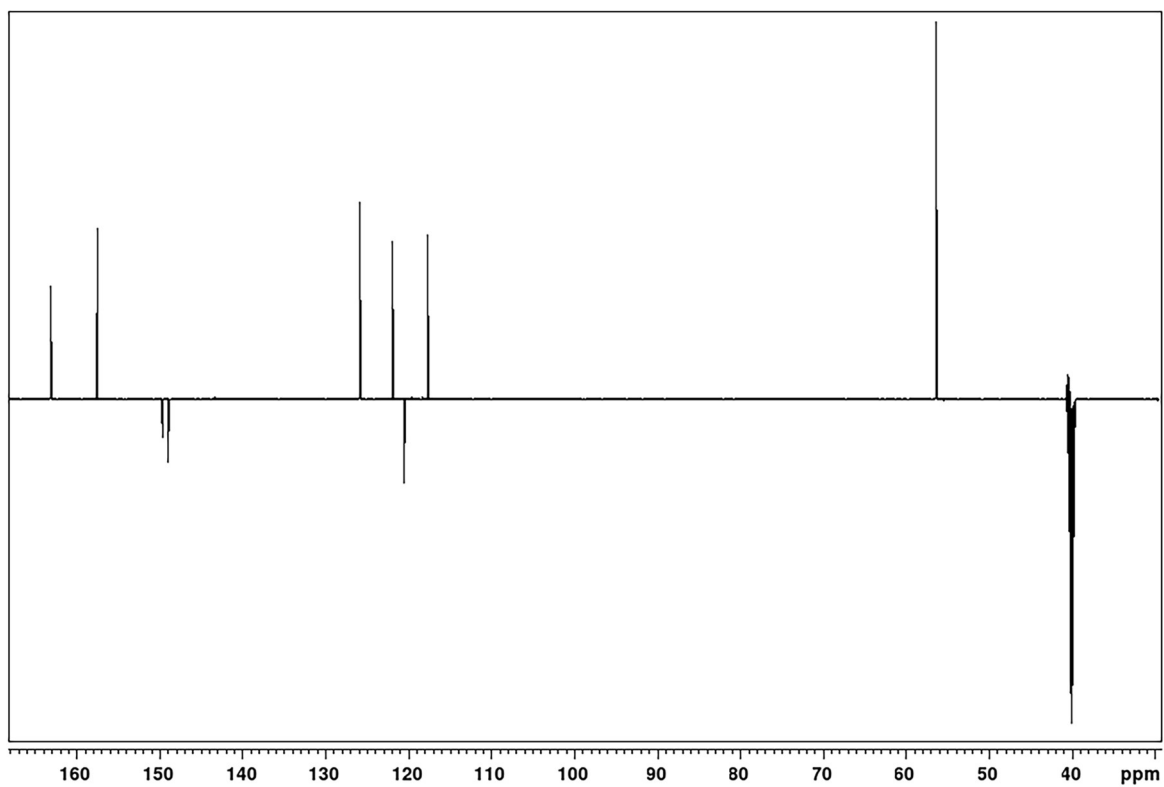


Figure S33. ^{13}C NMR spectrum of the complex $[\text{MoO}_2(\text{L}^1)(\text{H}_2\text{O})]$ (1)

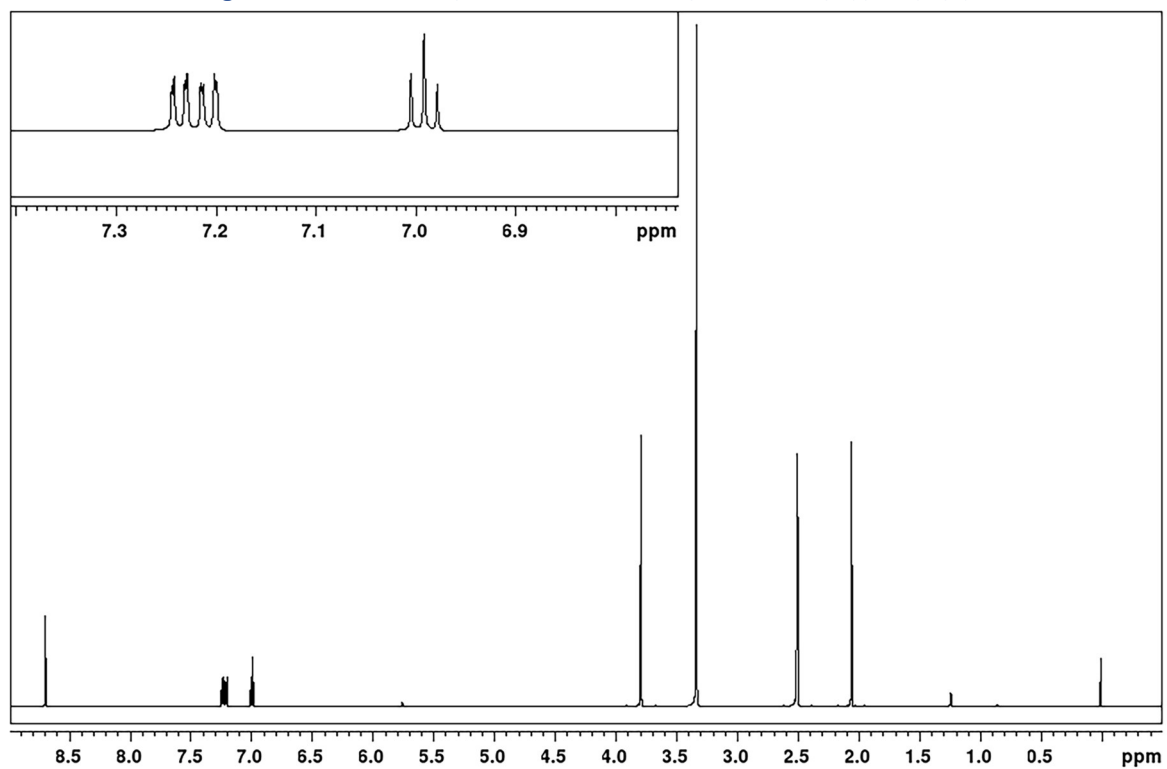


Figure S34. ^1H NMR spectrum of the complex $[\text{MoO}_2(\text{L}^2)(\text{H}_2\text{O})]$ (3) with an enlarged view of the signals at chemical shifts from 6.90 to 7.30 ppm

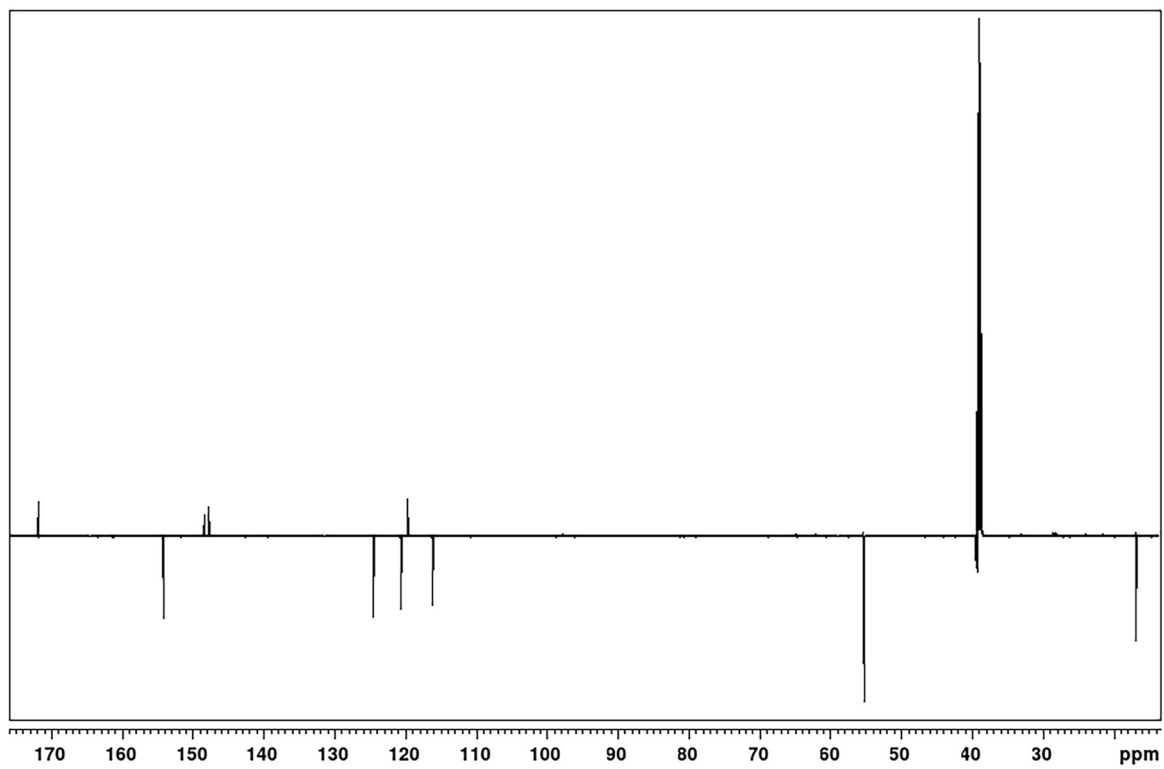


Figure S35. ^{13}C NMR spectrum of the complex $[\text{MoO}_2(\text{L}^2)(\text{H}_2\text{O})]$ (3)